Palacký University Olomouc
Faculty of Science
Joint Laboratory of Optics

MASTER THESIS

Characterization of semiconductor detectors for gamma-rays detection and their application in Mössbauer spectroscopy.

Author:	**Daniel Staník**
Study program:	N0533A110002 Applied Physics
Field of study:	1702T001 Applied Physics (AFYZ)
Form of study:	Full-time
Supervisor:	Mgr. Aleš Stejskal Ph.D.
Deadline:	May 2024

I would like to thank my supervisor Mgr. Aleš Stejskal Ph.D. for his support, guidance and feedback during the whole process of writing this thesis. I would also like to thank my former supervisor Mgr. Leo Schlattauer Ph.D. for the necessary support at the very beginning of the work on the experimental part of this thesis.

DECLARATION

I hereby declare that I elaborated this master thesis independently under the supervision of Mgr. Aleš Stejskal Ph.D., using only information sources referred in the Literature chapter.

In Olomouc May 14, 2024

. . . . . .

Daniel Staník

Bibliografická identifikace

Jméno a příjmení autora	Daniel Staník
Název práce	Charakterizace polovodičových detektorů pro detekci gama záření a jejich aplikace v Mössbauerově spektroskopii.
Typ práce	Diplomová
Pracoviště	Společná laboratoř optiky
Vedoucí práce	Mgr. Aleš Stejskal Ph.D.
Konzultant	Mgr. Leo Schlattauer Ph.D.
Rok obhajoby práce	2024
Abstrakt	Tato práce je věnována vývoji polovodičového detektoru pro nízkoenergetické gamma fotony. Popisuje testování PIN fotodiod, vývoj analogových elektornických obvodů pro gamma a Mössbauerovu spektroskopii a taktéž se zabývá komparačními měřeními mezi polovodičovými detektory a jinými typy detektorů.
Klíčová slova	PIN fotodioda, PCB, MS, gamma spektrum, předzesilovač
Počet stran	71
Počet příloh	1
Jazyk	anglický

Bibliographical identification

Autor's first name and surname	Daniel Staník
Title	Characterization of semiconductor detectors for gamma-rays detection and their application in Mössbauer spectroscopy.
Type of thesis	Master
Department	Joint Laboratory of Optics
Supervisor	Mgr. Aleš Stejskal Ph.D.
Consultant	Mgr. Leo Schlattauer Ph.D.
The year of presentation	2024
Abstract	This thesis is dedicated to the development of of semiconductor detectors for low energy gamma photons. It describes the testing of PIN photodiodes, the development of analog electronic circuits for the purposes gamma and Mössbauer spectroscopy and also deals with comparative measurements between semiconductor detectors and other types of detectors.
Keywords	PIN photodiode, PCB, MS, gamma spectrum, preamplifier
Number of pages	71
Number of appendices	1
Language	english

Contents

Introduction

In nuclear and particle physics, semiconductor-based detectors are becoming increasingly common due to the many unique properties they offer. Semiconductor detectors have a very wide range of applications, from spectroscopy to large particle experiments such as ATLAS at CERN.

This thesis is dedicated to the development of a semiconductor detector based on a Si photodiode for the detection of low energy gamma photons. The detection of low-energy gamma photons plays a crucial role in the field of Mössbauer spectroscopy, which requires a detector with sufficient detection efficiency and energy resolution.

The first four chapters are theoretical and provide a brief introduction to the mechanisms of gamma photon interaction and detection, the properties of semiconductor detectors and the basics of Mössbauer spectroscopy. These chapters are followed by a chapter describing the specifications of nuclear instruments used to build a spectrometric chain, and then a chapter introducing the numerical analysis of gamma energy spectra.

The experimental part begins with the gamma detection tests of selected photodiodes and is followed by a chapter filled with the technical description of the printed circuit board (PCB) integration of the spectrometric chain. The thesis ends with two chapters presenting the results of gamma energy spectra and Mössbauer spectra measurements.

Chapter 1

Gamma rays properties and matter interaction

1.1 Gamma radiation emission

Gamma rays are photons, but the main difference from X-ray photons is that they originate only from the atomic nucleus when it is de-excited from a higher energy level to a lower one. The energy levels of the nucleus are similar to the levels in the electron shell - discrete, characteristic for each isotope and can be described by quantum numbers. Alpha and beta decays produce a new nucleus in an excited state and are therefore followed by gamma emission.

1.2 Passage of radiation and particles through matter

Interaction of a particle (radiation) with another particle (atom, nucleus) or with condensed matter can result in many types of interactions and effects - scattering of a particle, creation of new particles and nuclei, annihilation of the incident particle, etc. It depends mainly on the energy, electric charge, spin and mass of the particle, but also on the properties of the target particle or matter. The physical quantity that describes the probability of a particular interaction between a particle and a target is known as the cross section. Normalised to the unit solid angle - differential cross section:

$$\frac{d\sigma}{d\Omega} = \frac{1}{F_{\text{part}}} \frac{dN_{\text{s}}}{d\Omega}, \tag{1.1}$$

where F_{part} is the particle flux, Ω is the solid angle and N_{s} is the average number of particles scattered per unit time. And the total cross section is given by integration:

$$\sigma = \int \frac{d\sigma}{d\Omega} d\Omega. \tag{1.2}$$

However, to characterise the interaction probability of a particle with condensed matter containing many interaction centres (defined by their density), other assumptions have to be made. The average number of scattered particles is given by:

$$N_{\text{sc}}(\Omega) = F_{\text{part}} A N_{\text{i}} \delta x \frac{d\sigma}{d\Omega} \tag{1.3}$$

and integrated over the entire solid angle:

$$N_{\mathrm{tot}} = F_{\mathrm{part}} A N_{\mathrm{i}} \sigma \delta x. \tag{1.4}$$

The A is the total area perpendicular to the flux, δx is the material thickness and N_{i} is the density of interaction centres.

Heavy charged particles (such as alpha particles, protons, muons, pions) lose energy mainly through collisions with atomic electrons. Due to their mass, which is much higher than the mass of the electrons ($M >> m_{\mathrm{e}}$) they collide with, the direction of their trajectory remains unchanged. The energy loss per unit distance is defined as the stopping power $\frac{dE}{dx}$. The stopping power for the heavy charged particles is given by the Bethe-Bloch formula, which relates the stopping power to the energy of the particle. However, the Bethe-Bloch formula doesn't apply at low energies (guided by Lindhard theory) and at higher energies (bremsstrahlung radiation). The change in path direction is possible, with a lower probability, by the secondary interaction - elastic scattering from nuclei.

Electrons and positrons have a much lower mass than the heavy charged particles, so the direction of their trajectory is changed by their movement in the electric field of the nucleus. The bremsstrahlung radiation losses are major yet at low energies. However, the energy lost in the collisions is also important - it is guided by the special Bethe-Bloch formula that takes into account the change in the direction of the path.

Other interaction effects are also possible (Cherenkov emission, nuclear reactions), but they are rare or do not affect the energy of the particle as much as those mentioned above. The interaction of neutrons is completely different because they have no charge. The interaction effects for gamma rays are described in more detail in the following chapter.

1.2.1 Gamma matter interaction

Due to the fact that gamma rays are photons, the gradual loss of kinetic energy within materials (characteristic of charged particles) is not observed. Instead, the main effect observed is the attenuation of the intensity of the photon flux with increasing thickness of the absorber material.

Three main interactions of photons with matter are: photoelectric effect, Compton scattering and pair production. The cross sections of these interactions vary with the gamma photon energy, the material and its density (strong dependence on the atomic number Z). Nuclear resonance interactions such as the Mössbauer effect are also possible, but their observation requires very special conditions.

The attenuation of the photon flux has a form of exponential decay:

$$I_{\mathrm{T}} = I_0 exp(-\mu x), \tag{1.5}$$

where I_0 is the incident radiation intensity, I_{T} is the transmitted radiation intensity and the parameter μ is the total absorption coefficient, which describes the probability of interaction per unit length and is bounded with the total cross section of single atom σ_{A} (combination of the cross sections of the three main effects) by the relation:

$$\mu = N_{\mathrm{d}} \sigma_{\mathrm{A}} = \sigma_{\mathrm{A}} (N_a \rho / A_{\mathrm{w}}) \tag{1.6}$$

where N_{d} is the atomic density, N_{a} is the Avogadro number, ρ is the material density and A_{w} is the molecular weight. The total cross section of the combined three main interactions as a function of photon energy for lead is shown in the figure 1.1.

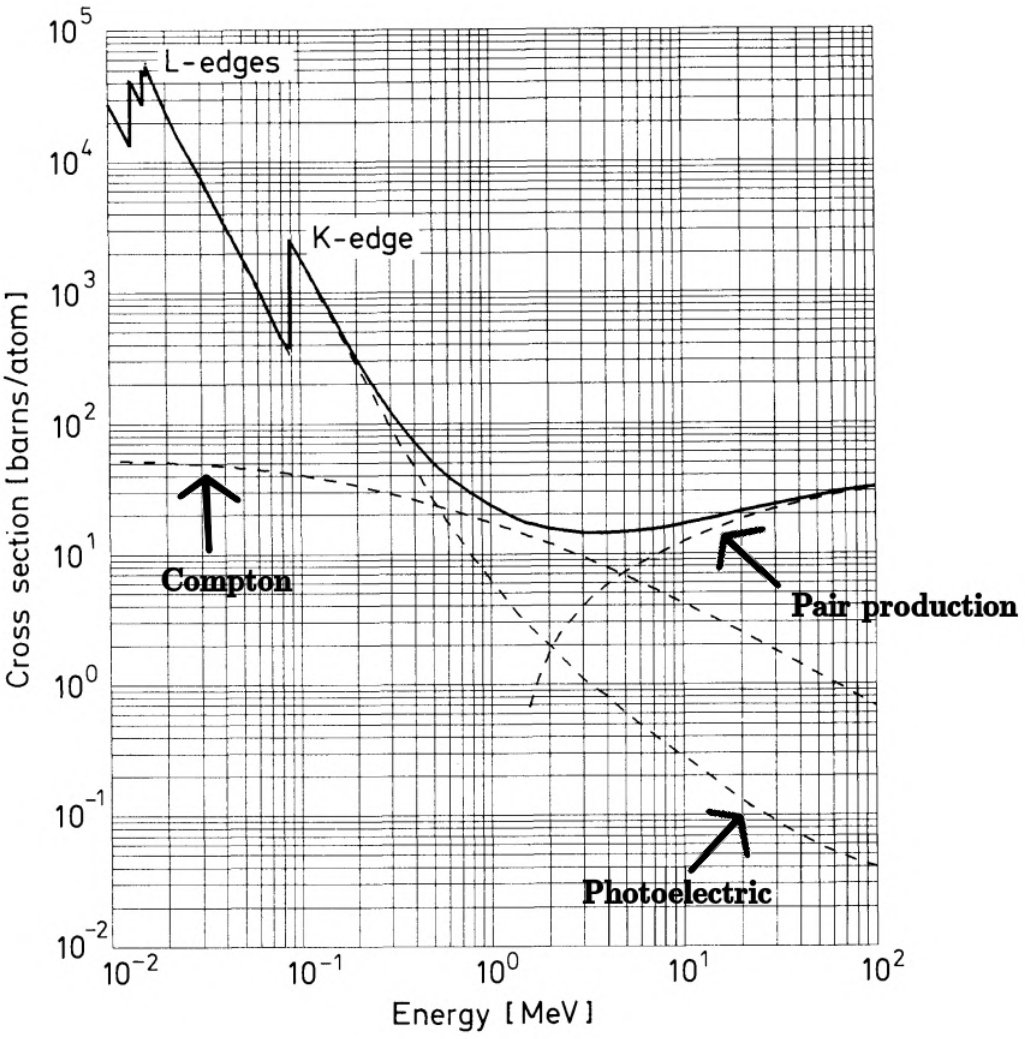

Figure 1.1: Example of total absorption cross section for high energy photons for lead. Taken and modified from [1].

Photoelectric effect

The photon is absorbed by an electron from the atomic shell. The electron is ejected and acquires the kinetic energy given by the well-known equation:

$$E_{\mathrm{e}} = hf - E_{\mathrm{b}}, \tag{1.7}$$

where f is the photon frequency and E_{b} is the binding energy.

The photoelectric effect can only be observed on electrons bounded in the atomic shell, because the nuclei can absorb the momentum of the photon. The cross section usually decreases with energy and can show characteristic discontinuities of K, L, M transitions. Two types of photoelectric effect can be distinguished - external and internal. External photoelectric effect results in the ejection of the electron out of the material - an effect observed in photocathodes. Internal photoelectric effect causes the electron to be excited to a higher energy level - in semiconductors this means from the valence band to the conduction band. The photoelectric effect plays a key role in the detection of gamma photons.

Compton scattering

Compton scattering is an effect mainly observed on free electrons. It must be said that the electrons in a material are usually bound, but if the photon energy is much higher than the binding energy, the electron can be considered free [1].

This effect causes the photon to lose only part of its energy and change direction. The energy is transferred to an electron according to the laws of conservation of energy and momentum, and can be described by the following relationship:

$$E_{\mathrm{e}} = E_1 - E_2 = E_1[1 - \frac{1}{1 + \frac{E_1}{m_{\mathrm{e}}c^2}(1 - \cos\theta)}], \tag{1.8}$$

where E_{e} is the energy transferred to an electron, E_1 is the initial photon energy, E_2 is the scattered photon energy, m_{e} is the the electron mass and θ is the scattering angle. This equation can be used to calculate the positions of Compton edges in energy spectra by plugging in the angle of maximum energy transfer ($\varphi = 180°$).

Pair production

At much higher energies, the photon can be converted into an electron-positron pair. This effect occurs near the nucleus, which absorbs a part of the original photon momentum [1]. Minimum required energy is 1.022 MeV, which corresponds to 2× electron rest energy.

The pair production and the electron bremsstrahlung are key effects in the development of electron-photon showers. If the electron/positron produced has sufficient energy, it emits bremsstrahlung photons. These bremsstrahlung photons can interact again via pair production, creating new electrons. This process of shower evolution continues until the energy of the electron/positron pairs falls below the energy required to produce bremsstrahlung radiation. At lower energies, the electrons lose more of their energy through atomic collisions than through bremsstrahlung.

Negative effects from this type of interaction, such as the creation of single and double escape peaks or annihilation peaks in spectra, are not observed because the cross section for low-energy gamma photons is very small. This means that this interaction can be neglected for the purposes of this thesis.

1.2.2 Characteristic energy spectra

Each gamma source emits photons with a characteristic energy with a certain probability. However, this characteristic energy can be altered by interactions that may occur in the environment or within the detector itself. This results in the registration of photon events with altered energies.

In the environment the energy spectra can be affected by:

- Characteristic X-rays - radiation-induced fluorescence usually from the shielding material (Pb).
- Backscatter peak - Compton scattering which occurred over a wide angle.

Inside the detector the energy spectra can be affected by:

- X-ray escape peaks - When the photoeffect occurs at atomic energy levels, the characteristic X-ray of the detector material is emitted. The escape peak has the energy of the captured photon minus the energy of the escaped X-ray.

- Compton continuum - the photon interacts inside detector by Compton scattering, the scattered photon leaves the detector, which registers the photon energy loss.

Chapter 2

Gamma rays detection

2.1 Properties and parameters of detectors

The main parameters of interest for Mössbauer spectroscopy are detection efficiency and energy resolution at low gamma energies. Nowadays, three main types of detectors are used in nuclear physics - gas, scintillation and semiconductor. The Mössbauer spectrometer setups in the laboratories of the Department of Experimental Physics (DEP) of Palacky University are usually based on gas or scintillation detectors.

2.1.1 Gas proportional detectors

The gas detectors are usually tubes with two electrodes filled with a special gas mixture. A gas tube LND45479, which will be used for experiments in the following chapters, is shown in the figure 2.1. The incoming particle ionises the gas, producing free ions and electrons. Gas detectors are operated in the proportional regime, which is characterised by proportional amplification of the charge carriers. The advantage of gas detectors is that they offer good energy resolution, but on the other hand their detection efficiency is low, mainly due to the fact that the gas density is low. Count rates are also affected by the long duration of the ionisation effect. They require high voltages (typically over 1000 V) to operate and, in the case of flow counters they also require pressure cylinders.

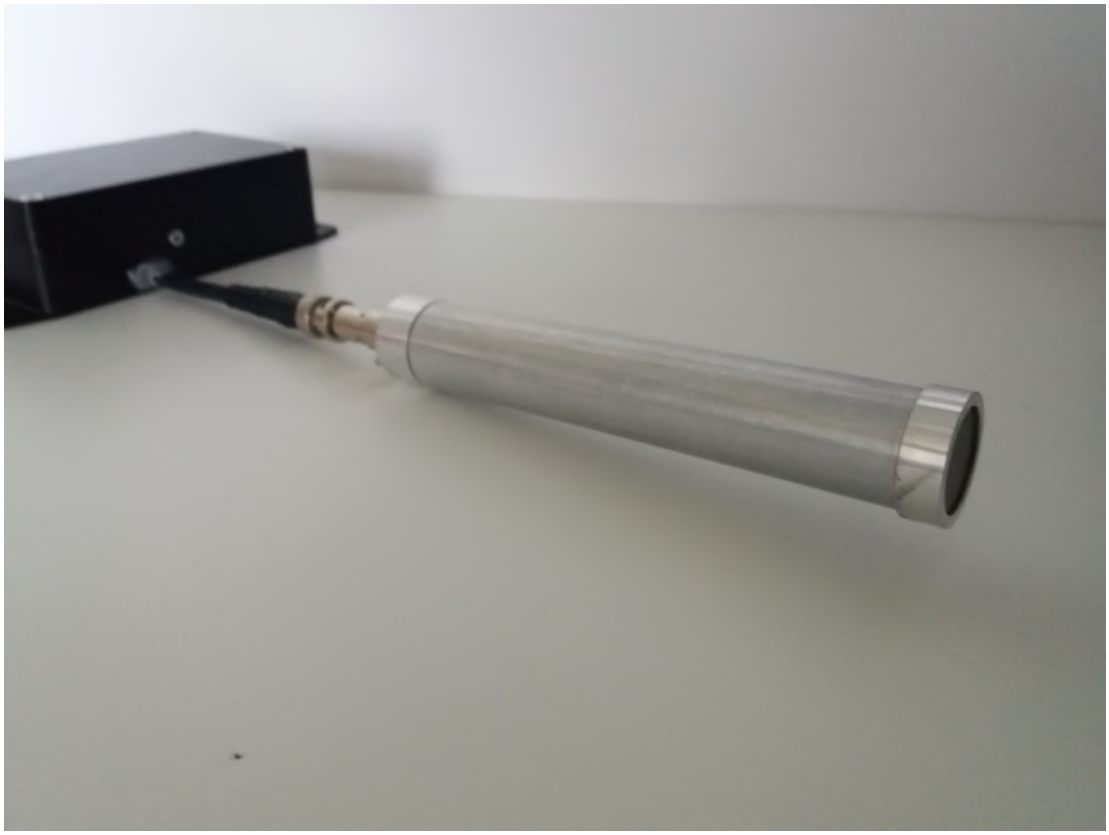

Figure 2.1: Gas proportional detector LND45479.

2.1.2 Scintillation detectors

A scintillation detector is usually a scintillation crystal coupled to a photomultiplier tube (PMT). A scintillation detector (PMT R6095 with YAP(Ce) crystal) used later in this thesis can be seen in the figure 2.2. The first conversion of photon energy takes place inside the scintillation crystal, where the incoming particle produces a number of photons linearly dependent on its energy. These photons are captured by the photocathode of the PMT, where they are converted into electrons and then amplified on the dynodes of the PMT. This amplification requires high voltages (from 500V). The gain inside the PMT can be around 10^6.

The detection efficiency is very high and, due to the short excitation time, they can be used at high count rates. However, their energy resolution is much worse than in the case of gas detectors and semiconductors. The resulting gamma spectra tend to have distorted broad peaks, which negatively affects Mössbauer spectroscopy - reduces SNR.

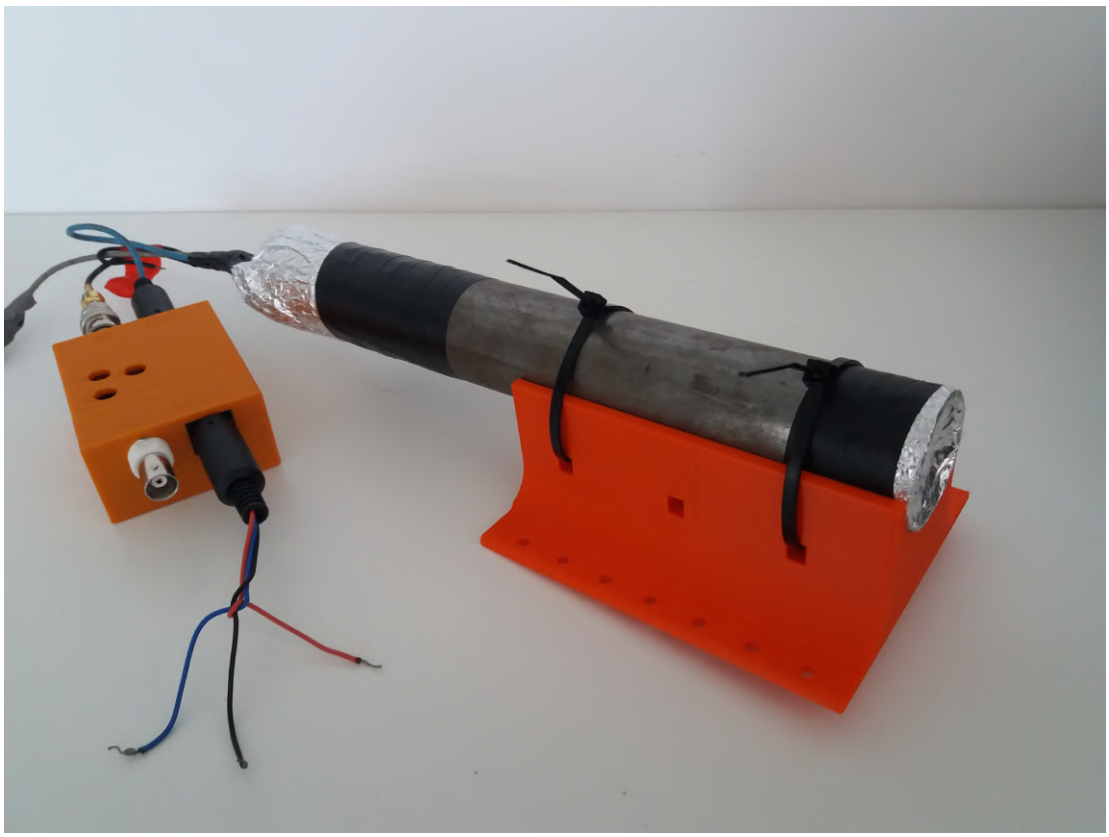

Figure 2.2: Scintillation detector with amplifier. PMT (R6095) and scintillation crystal (YAP(Ce)) are inside the metal tube.

2.1.3 Detectors based on semiconductors

Semiconductors offer the best energy resolution - the energy required to produce a charge carrier is usually very small (in the order of eV). Detection efficiency depends on the energy of the gamma photon and the thickness of the detector. The efficiency can be very high - for example, some Si PIN diodes have efficiencies close to 100 % up to 10 keV [2].

However, semiconductors are usually more expensive than the other types of detectors. They can be used as direct radiation detectors, or they can be coupled with a scintillator crystal.

One problem with semiconductor detectors is that there is no internal amplification, so the signals coming out of the detectors have to be heavily amplified by electronics. On the other hand, they are small and compact. They also don't require high voltage sources or heavy pressure cylinders to operate. These facts are crucial when it comes to building more compact Mössbauer spectrometers - for example, MIMOS II [3], based on 4 Si PIN diodes, was part of the two rovers Spirit and Opportunity on their mission to Mars.

Chapter 3

Semiconductor detectors with p-n junction

Semiconductor structures have unique properties that make them useful for more than just particle/photon detection. There are many types of semiconductor detectors, starting with conventional photoresistors and photodiodes for light intensity measurements with a spectral range from infrared to UV. For low intensities and single photon events there are avalanche photodiodes (APDs). When the whole image needs to be captured, matrix detectors such as CCD and CMOS cameras can be used. In nuclear and particle physics, semiconductor detectors for X-rays, gamma rays and other particles are becoming increasingly common. For more complex measurements, such as particle trajectories, matrix drift or strip detectors may be the right choice. For gamma spectroscopy, p-n junction detectors are essential. To detect Mössbauer 14.4 keV gammas our primary choice are the Si PIN diodes for direct detection due to the high detection efficiency under 25 keV [2].

3.1 The structure of semiconductor

Individual atoms are characterised by the well-known discrete energy levels, but in the case of solid crystals there is another model to describe the energy levels - the band structure. In this model, the energy levels are so close to each other that they almost form a continuum. This difference in behaviour is due to a periodic potential within the crystal lattice. However, the electron energy E_c is not the only quantum number that describes the behaviour of electrons within the periodic potential. By solving the Schrödinger equation using the so-called Bloch theorem, we conclude that the second important quantum number is the wave vector $\boldsymbol{k}$. These two quantum numbers are bounded by the dispersion relation $E_c = E_c(\boldsymbol{k})$, which is characteristic of each crystal and may play a role in the transition of electrons between bands.

3.1.1 Direct and indirect semiconductors

The shape of the dispersion relations $E_c(\boldsymbol{k})$ divides the semiconductors into two categories - direct and indirect semiconductors. For direct semiconductors the energy minimum in the conduction band and the energy maximum in the valence band have the same $\boldsymbol{k}$, so the transition can occur after the E_g is supplied. In the case of indirect, the minimum and maximum have different $\boldsymbol{k}$. To make the transition, additional

momentum must be supplied (e.g. by phonons) or the energy supplied must be much greater to allow the transition to the higher state with the same $\boldsymbol{k}$.

3.1.2 Band structure

The basic difference between conductors, insulators and semiconductors is the valence and conduction band structure. In conductors, the valence band overlaps the conduction band. The electrons in the conduction band can move almost freely throughout the crystal. For insulators, there is no overlap and the energy gap E_{g} between the two bands is so large that it makes any electron transitions almost impossible. However, in the case of semiconductors, the E_{g} is small enough to allow the electron to jump into the conduction band and leave the hole in the valence band after receiving enough energy - in the form of thermal energy $E_{\mathrm{T}} = kT$, electric field $E_{\mathrm{s}} = -e\phi$ or photon $E_{\mathrm{photon}} = \hbar\omega_{\mathrm{photon}}$. The last one is the most important because it allows us to use semiconductors as detectors. Both the electron and the hole take part in the conduction.

3.1.3 Occupation of states

The occupation probability of states in the band structure is given by the Fermi-Dirac distribution, since the electrons are the fermions with the exclusion rules. The possible occupied state where the occupation probability falls below 50 % is called the Fermi level with Fermi energy E_{F}. For an ideal pure semiconductor at $T = 0$ K the E_{F} is in the centre of the band gap. With increasing temperature the Fermi level in most materials moves upwards towards the conduction band.

3.1.4 Semiconductor Crystals

Semiconductor materials are usually in the form of a crystal with a diamond structure (two FCC lattices bonded together), where the lattice atoms are bonded together by a covalent bond. However, in real crystals there are also defects and impurities that can change the functionality. The impurities can be intentionally added to enhance the desired properties in a process called doping.

There are several suitable materials for the construction of ionising radiation detectors. Among them the well-known is Ge, which has very good energy resolution but requires cooling. Another suitable material is Si. Si photodiodes have a high detection efficiency below 25 keV and are easy to manufacture, since many other semiconductor devices are made of Si. In the case of wide-spectrum X-ray and gamma-ray detectors, CdTe can provide sufficient parameters. The manufacture of semiconductors for detection purposes involves many complicated processes because the detector requirements for crystal purity are very high.

3.2 The p–n junction

Intrinsic semiconductors have a limited range of applications. We can alter the behaviour by adding specific impurities and create an extrinsic semiconductor. The Si atom has 4 valence electrons which form a covalent bond with other Si atoms. If the Si atom is replaced by an atom with 5 valence electrons, one of them will have a very

weak bond. By doping the intrinsic semiconductor with these atoms we create the n-type with additional electrons localised almost in the conduction band. However, the crystal as a whole remains neutral. Similarly, doping with atoms with only 3 valence electrons will create holes in the valence band - the p-type. These atoms create energy levels in the band structure, but at room temperature they are all mostly ionised and participate in conduction. The full theoretical treatment of doping is very complex, taking into account many other quantum and statistical physics aspects, and is not useful for the purposes of this thesis.

The special effects arise when p-type and and n-type are bound together. The holes of the p type and the electrons of the n type will start to diffuse into the other region. However, this movement alters the charge density, leading to the creation of a built-in voltage, which in the end cancels out the diffusion. This creates the depleted region, where there are no free carriers.

Another theoretical view is that the electrons will rearrange because the Fermi level must be the same throughout the crystal, whereas for the stand-alone p type the Fermi level is closer to the valence band and for the n type closer to the conduction band. The potential created in this way equalises the different Fermi levels.

The p-n junction can be connected to the supply voltage (known as a bias) in two ways. The first possibility is the forward connection - the p layer to plus and n to minus. Increasing the voltage in this type of connection causes the size of the depleted layer to decrease until it disappears completely (bias voltage is opposite to the built-in voltage). The absence of the depleted layer makes the p-n junction conductive. The second possibility is the reverse - p to minus and n to plus. Increasing the voltage also increases the size of the depletion layer (bias goes with the built-in voltage). Since the size of the depletion layer is crucial for detection, semiconductor detectors are operated in reverse connection.

The p-n junction has many unique properties that are commonly used in the form of classical diodes. However, it is also crucial for detection because the free carriers (if produced at all) in the depleted layer are pushed towards the electrodes by the electric field and form a photocurrent.

For design purposes in electronic circuits, detectors are usually modelled as classical p-n diodes connected to the bias source in the reverse direction. In the case of detection, the detector can also be modelled as a current source.

The p-n junction has its characteristic capacitance, which depends on the size of the depleted layer and therefore on the bias voltage. This capacitance plays an important role as it affects the dynamic parameters of the detection circuits and modifies the overall frequency spectra.

3.3 Detection mechanism

The detection of a particle or photon is based on its interaction with the detector material - in semiconductors the formation of electron-hole pairs is observed. This can be achieved by the interaction mechanisms described in previous chapters, which differ for each type of particle and energy. In the case of low energy gamma, the two main mechanisms involved in the production of charge carriers are the photoeffect (internal) and Compton scattering.

The main purpose of the semiconductor as a detector is to perform a linear conversion of the particle/photon energy into the free charge carriers - electrons in the conduction band and holes in the valence band. The average energy required to create

a single electron-hole pair is usually a fixed constant - in Si it is $\epsilon = 3.6$ eV [4]. Since Si is an indirect semiconductor, this value is not equal to the gap energy, which is lower ($E_{\mathrm{g}} = 1.12$ eV).

The gamma photon hitting the detector first interacts with a single electron. When the photoeffect takes its place, the primary electron with an energy much higher than the thermal excitation will ionise electrons from all over the valence band, pushing them into higher states from the conduction band. These conduction band electrons de-excited to lower conduction band states and the holes redistributed to the upper valence band states. This de-excitation process releases energy and leads to a cascade of further excitations and interactions, producing many electron-hole pairs - the charge cloud. The number of generated electron-hole pairs n is simply given by the relation:

$$n = \frac{E_{\mathrm{gamma}}}{\epsilon}. \tag{3.1}$$

Compton scattering results in energy distortion and gamma spectrum degradation. Compton without any other subsequent interaction (Compton again or photoeffect) is typical for thin detectors because there is not sufficient thickness to stop the scattered photon again.

An ideal very thick detector could solve this problem, because all possible interactions and all subsequent sub-interactions would take place inside the detector, resulting in electron-hole generation. Such a detector would have only the full energy peaks without any other unwanted counts. However, the construction of such a detector is very complicated due to the many technical and manufacturing problems that arise with increasing dimensions.

In a p-n junction, the charge carriers generated in the depleted layer are pushed towards the electrodes by an internal electric field. The electronics accumulate the charge and convert it into a voltage pulse signal, which is then analysed to extract the energy information. Since the depleted layer is the only part where detection can occur, it is obvious that it should be as large as possible for detector purposes.

To achieve the larger dimensions of the detection part, the p-n junction can be upgraded to a p-i-n junction, which contains an additional intrinsic layer between the p and n parts, acting as a fixed size depleted layer. The detectors with p-i-n junction are called PIN photodiodes. The additional intrinsic layer reduces the capacitance but increases the time it takes for charge carriers to leave the detector.

3.4 Main noise sources and resolution limitations

Detection efficiency and energy resolution are strongly affected by noise that alters the signal. While some negative effects are caused by outside conditions such as temperature or by noise in the electronics, some originate strictly from the properties of the semiconductor material and can only be minimised during the preparation of the crystal.

3.4.1 Fano noise

The physical effect within the semiconductor itself that limits the measured energy resolution is the fact that not all of the particle's energy is converted into charge carriers. A fraction of the energy can be consumed to induce lattice vibrations (phonons).

Statistically, the relative resolution can be described by the following equation:

$$\frac{\Delta E}{E} = 2.35\sqrt{\frac{F\epsilon}{E}}, \tag{3.2}$$

where E is the energy of the incoming particle, ϵ is the average energy required to produce a single pair, and F is a Fano factor. The Fano factor is a special statistical constant that describes the dispersion in the counting process. If we consider the case of 14.4 keV gamma in Si ($\epsilon = 3.6$ eV, $F = 0.12$), the $\frac{\Delta E}{E}$ is equal to 1.3 % and ΔE is 185.4 eV. This resolution is sometimes called intrinsic, because the real resolution is much worse.

3.4.2 Thermal noise

It has been mentioned that the electrons can also be excited by thermal fluctuations. However, since many of the detector materials are indirect semiconductors, the thermal excitations are carried by the intermediate states within the band gap. These states originate from imperfections and impurities in the crystal lattice. The electrons and holes originating from this effect can join the charge cloud generated by the detected particle and reduce the SNR. This phenomenon is commonly referred to as dark current. Dark current is also increased by an applied bias.

Thermal fluctuations are much more significant for materials that require less energy to excite the electrons to the conduction band, such as Ge. These detectors must always be operated at low temperatures. Even room temperature can lead to the breakdown and destruction of a detector. For Si, the valence and conduction bands are further from each other, so thermal fluctuations are not as critical.

3.4.3 Recombination and trapping

The effect that counteracts successful carrier collection, and thus affects detection efficiency and energy resolution, is recombination. In pure crystals, the electron can only recombine with a hole if they have the same $\boldsymbol{k}$. However, in real crystals there are impurities that allow carriers to recombine - recombination centres. The charge collection must take much less time than the carriers need to recombine.

Another effect caused by the same impurities is trapping. The trapping centres capture the electron or hole and release it after a certain time. This effect alters the signal pulses and can reduce the maximum possible counting rate.

Energy levels near the centre of the band gap are primarily responsible for recombination and trapping, which means that the impurities causing this are not the impurities added by doping, as these have their extra energy levels near the bands.

3.5 Structure and parameters of Si PIN detector

One of the most important parameters is the size of the photosensitive area, which must be as large as possible for effective radiation collection. This area must be treated with extreme care, as any damage, adsorption of impurities or condensation due to high ambient humidity will reduce the active photosensitive area.

For detection purposes, the dimensions of all three layers (P, I and N) of the p-i-n semiconductor structure must be carefully designed. Obviously, the most important

layer dimensions for the interactions within the detector are those parallel to the direction of incident radiation - the thicknesses of both the P and I regions. The dead region (P) must be as thin as possible to reduce the probability that the particle will interact at a location where the generated charge cloud would recombine almost immediately. The active depleted layer (I) must be thick enough to allow all interactions to take place within itself. The schematic of a PIN photodiode can be seen in the figure 3.1.

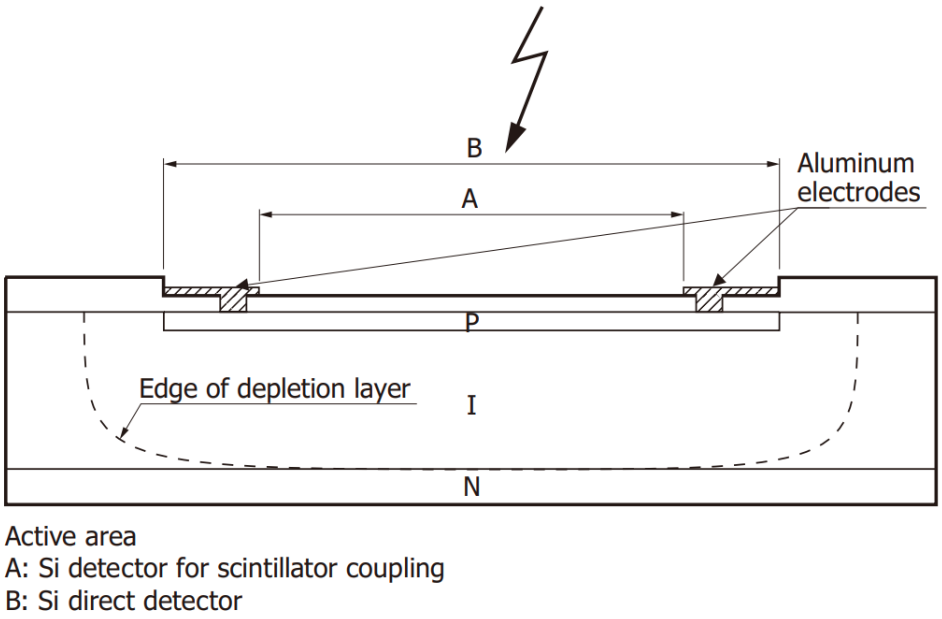

Figure 3.1: Cross section of Si detector for scintillator coupling and Si direct detector [5].

3.6 Available Si PIN detectors

For testing, we chose a professional Hamamatsu S14605 PIN diode and two commercial PIN diodes: BPW34 - visible and near infrared radiation detector, OPF430 - originally designed for use in optical communications.

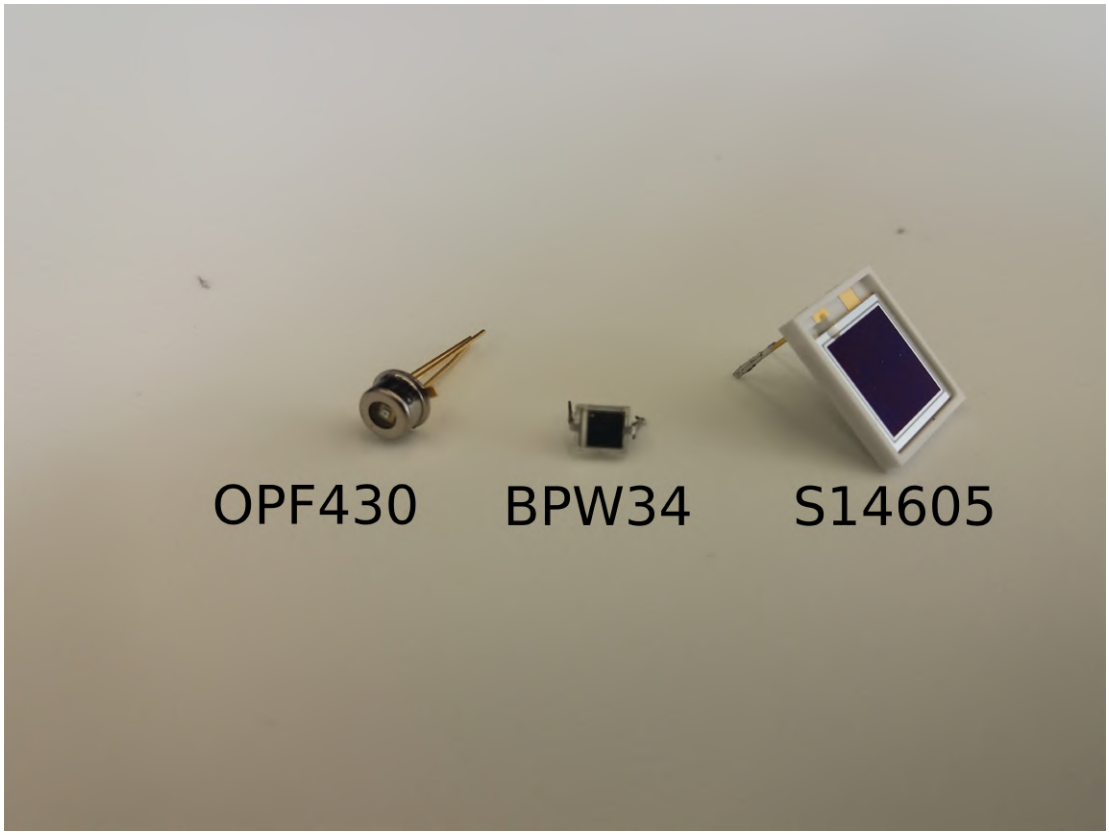

Figure 3.2: PIN diodes - OPF430, BPW34 and S14605.

3.6.1 Hamamatsu S14605

The professional S14605 is designed for use as a direct radiation detector. It has a very large light sensitive area and low capacitance.

Parameters [6]:

- Maximum reverse voltage U_R: 150 V
- Photosensitive area: 81 mm^2
- Capacitance: 25 pF at $U_R = 100$ V
- Dark current: 8 nA at $U_R = 100$ V
- Depletion layer: 0.5 mm
- Cost: 5000 CZK

3.6.2 BPW34

BPW34 is a very inexpensive radiation detector. There was a manual [7] on how to use BPW34 as a beta particle detector, and since it is a Si PIN diode, it is worth a try and test for our gamma detection purposes.

Parameters [8]:

- Maximum reverse voltage U_R: 32 V
- Photosensitive area: 7.5 mm^2

- Capacitance: 25 pF at $U_{\mathrm{R}} = 3$ V
- Dark current: 2 nA at $U_{\mathrm{R}} = 10$ V
- Depletion layer: not specified
- Cost: 11 CZK

3.6.3 OPF430

OPF430 was originally intended as a low cost detector for fibre optic applications. However, there was a publication [9] which described the possibility of using similar diode OPF420 in low energy gamma spectroscopy chains as a low cost detector.

Parameters [10]:

- Maximum reverse voltage U_{R}: 100 V
- Photosensitive area: not specified, smaller than BPW34
- Capacitance: 1.5 pF at $U_{\mathrm{R}} = 5$ V
- Dark current: 0.1 nA at $U_{\mathrm{R}} = 5$ V
- Depletion layer: not specified
- Cost: 340 CZK

Chapter 4

Mössbauer effect and spectroscopy

The Mössbauer effect is an interaction that can occur on atomic nuclei under certain circumstances. It is a recoilless resonance emission/absorption of gamma photons by nuclei of the source/absorber with discrete nuclear energy levels. This effect has a special application in material science - Mössbauer spectroscopy (MS), which is a nuclear experimental technique and a special type of gamma spectroscopy that uses the appropriate nuclei in the sample as probes of local electric and magnetic fields.

This technique is capable of providing much unique information in material science, geology, chemistry and biology - study of phase and chemical composition of solid materials, study of local magnetic fields and spin states and in-situ measurements of phase transitions [11]. The main disadvantage of this technique is that there is no suitable radiation source for many isotopes. The most important is iron and its isotope ^{57}Fe with the radioactive source ^{57}Co (which decays to an excited state of ^{57}Fe with a half-life of 271.81 days [12]), which allows Mössbauer spectroscopy to be used in many areas studying iron compounds.

4.1 Physical concept

4.1.1 Resonace emission and absorption

In the previous chapters it was mentioned that atomic nuclei are quantum systems with discrete energy levels (analogous to the energy levels of the electron shell), so upon de-excitation or excitation they emit/absorb gamma photons with energy E_0 equal to the difference between the levels. The emitted/absorbed energy spectra follow the shape of the Lorentzian curve.

However, these emitted/absorbed energy spectra are altered due to the momentum conservation law. Part of the gamma photon energy is transferred to the kinetic energy of the nucleus, the crystal as a whole body, or transformed into lattice vibrations (phonons). In the case of a free, stationary nucleus, the momentum and energy transfers are so large that the emission and absorption spectra are shifted in different directions by large energetic values, making resonance absorption impossible to observe. However, the case of the nucleus bounded in the crystal lattice is different - the crystal as a whole body will absorb the momentum. If we consider that the whole crystal has a much larger mass than the nucleus, the energy transfer into the kinetic energy of the crystal will be negligible - the gamma photon energy remains unchanged and this results in recoilless emission/absorption. In this case the emission and absorption energy spectra overlap and this makes resonance absorption (Mössbauer effect) observable [11].

4.1.2 Interaction of nuclei with local fields

The nucleus, bounded within the lattice and surrounded by electrons arranged according to the chemical bonds, has perturbed energy levels. These perturbed energy levels are a consequence of the interactions of the nucleus with local electric and magnetic fields, resulting in each phase or chemical composition having its own nuclear emission/absorption spectrum - the Mössbauer spectrum. Quantum physics has very well known calculation techniques to describe these variations in energy spectra - perturbation theory.

The main properties of a nucleus that cause the interactions with local electric and magnetic fields are: the atomic number Z, the quadrupole moment Q_{n} and its spin I_{n} along with its projections. For spectroscopy there are three main hyperfine interactions [11]:

- Electric monopole interaction - the interaction between the protons of the nucleus and the s-electrons (which have a non-zero probability of being in the nucleus). It results in an isomeric shift of the energy levels $\delta = E_M - E_0$. The δ must be defined with respect to a fixed energy level, for example the level of the radioactive source that is used. This type of MS spectrum has a shape consisting of only one Lorentzian (singlet shape).

- Electric quadrupole interaction - the inhomogeneous electric field inside the nucleus interacts with the quadrupole momentum Q_{n} of the nuclei. It results in energy variations with respect to the square of the magnetic quantum number $E_{\mathrm{Q}} \sim m^2$ - the states allowing different values of $|m|$ are split into sub-states. For $m = \pm 1/2$ there are two Lorentzians in the MS spectra - dublet.

- Magnetic dipole interaction - the spin I_{n} is tied to the magnetic momentum by the relation $\mu_{\mathrm{m}} = \gamma I_{\mathrm{n}}$, where γ is a gyromagnetic ratio. This magnetic momentum interacts with magnetic fields in the nucleus and leads to the nuclear Zeeman effect - the splitting of states with respect to possible values of the magnetic quantum number m. The magnetic dipole interaction plays an important role in studying the magnetic properties of materials.

Each of these effects can occur separately or simultaneously with the others.

4.2 Mössbauer spectroscopy

To obtain the spectra, we can use one of several measurement setups with given geometries. In laboratories there are dominant the setups employing transmission or backscattering geometry with the sample as the absorber and with Doppler modulation of the gamma photon energy. The emitted photons or other products generated by the excitation are detected by a detector with electronics to accumulate the Mössbauer spectra. The source is attached to the Doppler modulation unit (transducer) and the energy of the gamma photons is modulated by the relative velocity of the source and absorber, typically in the range of about $\pm$ 1 μeV.

For the transmission geometry, the key concept of the measurement is that if we irradiate the sample placed as an absorber with gamma photons with energy varied by the Doppler modulation, the gamma photons with energy equal to one of the transitions (resonance energies) will be absorbed with a certain probability. The detector

is positioned behind the absorber and measures the number of gamma photons at a defined energy step. The minimum counts are measured around the resonance energy. The transmission geometry of Mössbauer spectra can be seen in the figure 4.1.

The concept of a backscattering geometry is similar in many ways, but the main difference is the detection of the secondary particles. The nuclei in the sample are excited by appropriate gamma photons and subsequently decay back to the original state with some effects following - re-emission of the "original" gamma photons in a random direction, emission of electrons from the shell (ejected by deexcitation energy quanta, also called conversion electrons) followed by characteristic x-rays or possibly by auger electrons. The detection of electrons and X-rays instead of gamma photons has many advantages and disadvantages, and for certain applications the use of the backscattering geometry may be more appropriate. For example, the detection of conversion electrons could handle the surface characterisation of the sample due to the lower transmittance of electrons when compared to gamma photons.

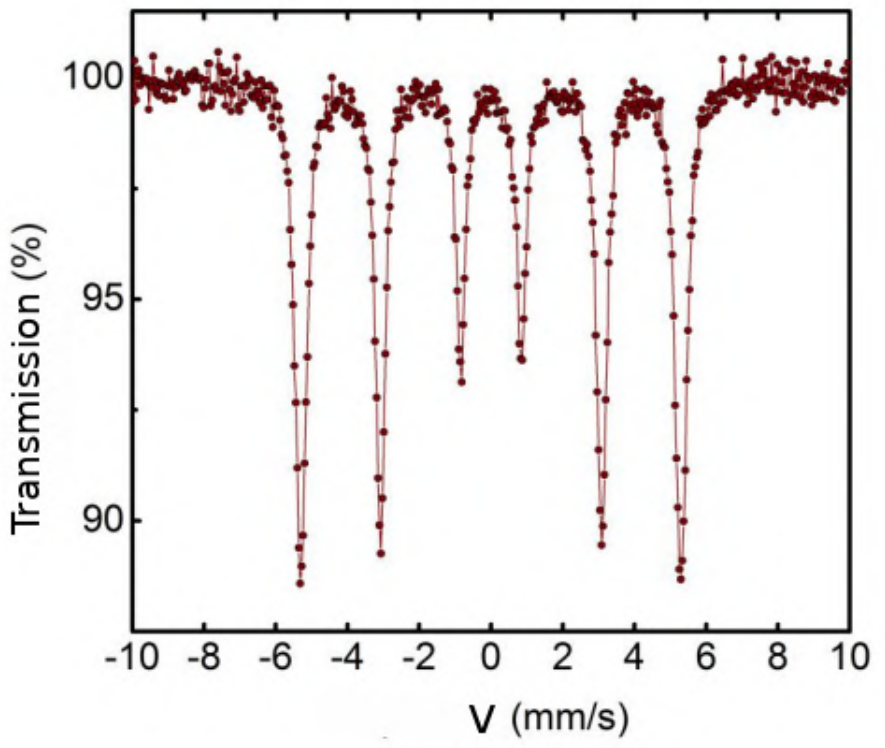

Figure 4.1: Transmission Mössbauer spectrum of α-Fe. Taken and modified from [13].

4.3 ^{57}Fe spectroscopy

One of the isotopes on which we are able to observe a Mössbauer effect is ^{57}Fe (relative abundance only 2.119% [14]). The source is ^{57}Co, which decays into the second excited state of ^{57}Fe by electron capture. The resulting ^{57}Fe nuclei can deexcite themselves in two ways (figure 4.2) - by direct deexcitation to the ground state by emission of 136.5 keV photon or by deexcitation to the first excited state by emission of 122.1 keV photon. The first excited state is essential as it is used to study the hyperfine interactions. After the lifetime of the first excited state, the 14.4 keV photon (or other possible conversion products) is emitted as it falls to the ground state. The ^{57}Fe spectroscopy in transmission geometry is based on the detection of the 14.4 keV gamma

photons. This thesis is mainly devoted to the application of semiconductor detectors for the detection of these 14.4 keV gamma photons. The ^{57}Fe spectroscopy can also be performed in the backscattering geometry by detecting the conversion electrons or conversion X-rays with energies around 6.4 keV.

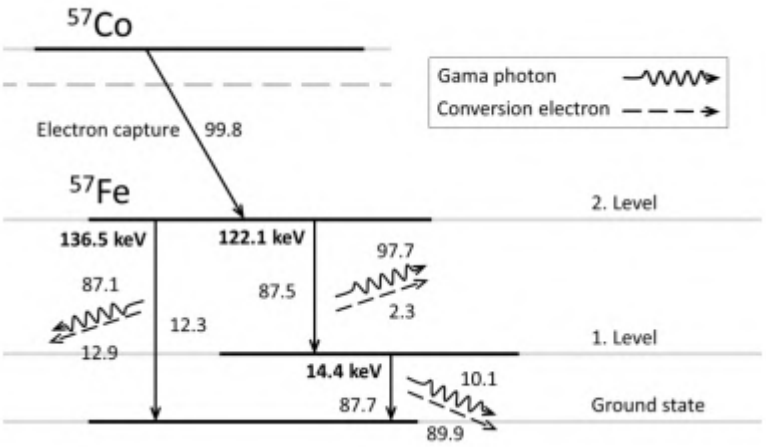

Figure 4.2: Decay scheme of ^{57}Co, taken from [13].

The MS spectrometer setup consists of several parts:

- Source of 14.4 keV gamma - ^{57}Co radioactive nuclei built into a crystal lattice (usually in a rhodium matrix). The source is mounted on the transducer.
- Transducer for Doppler modulation (figure 4.3). It usually consists of two coils surrounded by permanent magnets - one to drive the Doppler energy modulation and the other to measure the velocity [15]. The system is driven by PID (proportional integral derivative) or MPC (model predictive control) controllers for precise velocity and energy control. The speed can be either constant or with constant acceleration.
- Detector of transmitted/backscattered gamma radiation, conversion electrons or X-rays together with readout and evaluation electronics including amplifiers, single or multi-channel analysers, etc. It should also be noted that the conventional detectors mentioned above do not have sufficient energy resolution to distinguish the energy of perturbed states. For this reason, the count rates are synchronised with the Doppler energy modulation (actual modulated energy of the source), which is used to address the channels for spectrum accumulation.

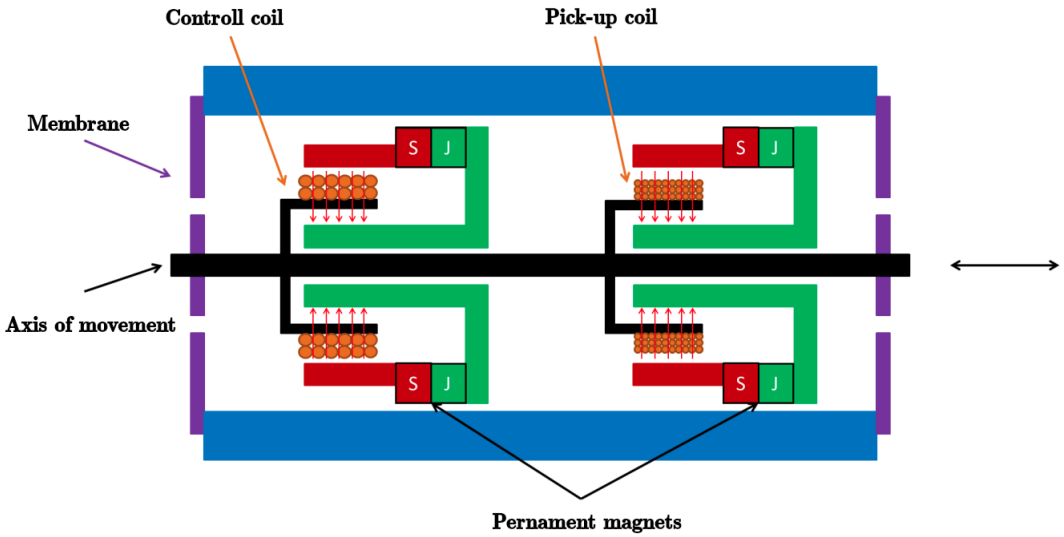

Figure 4.3: Transducer, taken from [16].

The diagram of the MS setup can be seen in the figure 4.4.

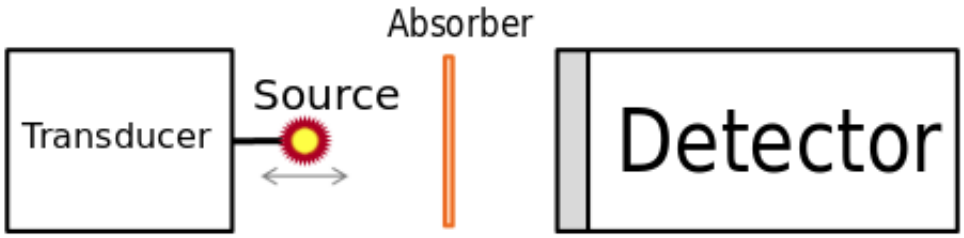

Figure 4.4: Diagram of the MS setup, taken and modified from [13].

4.4 MS spectra effect and SNR

The shape of the MS spectra can be modelled by Lorentzian curves. The singlet spectra in transmission geometry can be modelled by a single Lorentzian curve of the following form:

$$L(v) = -I_{\mathrm{MS}} \frac{(\frac{\Gamma}{2})^2}{(v - v_0)^2 + (\frac{\Gamma}{2})^2} + B, \tag{4.1}$$

where I_{MS} is the amplitude, the Γ is the FWHM, the B is a background level and v is the relative velocity of the radiation source and sample. The Lorentzian in this form has the associated area A equal to:

$$A = \pi I_{\mathrm{MS}} \Gamma \tag{4.2}$$

There are two properties of MS spectra that characterise their quality: SNR and the effect E_{MS}. They can be calculated from the spectrum parameters using the following equations:

$$\mathrm{SNR}_{\mathrm{MS}} = \frac{I_{\mathrm{MS}}}{\sqrt{B}} \tag{4.3}$$

$$E_{\mathrm{MS}} = \frac{I_{\mathrm{MS}}}{B} \tag{4.4}$$

Chapter 5

Electronics for signal readout and analysis

The signals coming out of the detector need to be properly pre-amplified, amplified and shaped. This task requires special analogue circuits with a properly designed layout. The measurement chain for gamma spectroscopy is usually realised in the following order - gamma detector, preamplifier, amplifier, multichannel analyser (MCA), microprocessor/computer (figure 5.1). When designing this spectrometric chain, we select components to achieve sufficient parameters for a particular application - in our case, energy resolution. For our spectrometric chain we chose instruments, modules and parts from two companies - ORTEC and CREMAT.

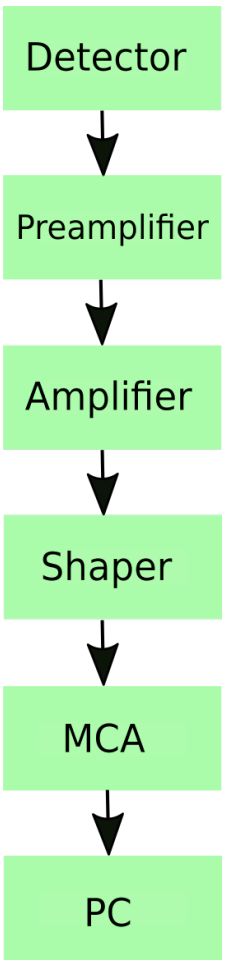

Figure 5.1: Spectrometric chain.

The task of realising the spectrometric chain can be accomplished in two ways. The first and simpler way is to build it from stand-alone robust instruments and modules. The second way is to design a printed circuit board (PCB) with the required functionalities from electronic components. In this thesis we use both methods for the development.

Building the chain from stand-alone instruments can be a more practical approach for testing the detectors themselves, as we are not forced to solve problems arising from the design of the electronic circuit board. However, these modules are usually very expensive, the measurement setups build this way are unnecessarily large and have worse noise parameters than electronic circuits specially tailored for the given application.

The PCB design requires a lot of electronic engineering skills and development time. The analog PCBs are very difficult to design. The advantages are that the final product can be very compact and cheap to manufacture.

5.1 PIN detector connection and bias voltage

5.1.1 Voltage source

The PN and PIN detectors require a voltage bias to reduce the capacitance. These voltage sources don't need to be stiff as the current consumption of the detector is very low.

Gas and scintillation detectors usually require high voltage sources (hundreds or thousands of volts). These high voltages are usually delivered by switching power supplies. However, these supplies are usually very noisy, and since semiconductors can be operated at much lower voltages, they are not needed. The better alternative is to use charge pump built of capacitors and diodes, which require lower frequencies to operate.

5.1.2 Shielding and grounding

Electromagnetic shielding is a very important part of sensitive analog signal circuits. Sensitive circuits must be surrounded from all sides by a metallic material, which must also be correctly connected to GND (the principle of the Faraday cage), otherwise correct operation cannot be guaranteed. The electromagnetic disturbance usually induces currents in the shielding material, so special care must be taken to prevent these currents from flowing through the signal routes. The figure 5.2 shows the difference between correct and incorrect shield connection.

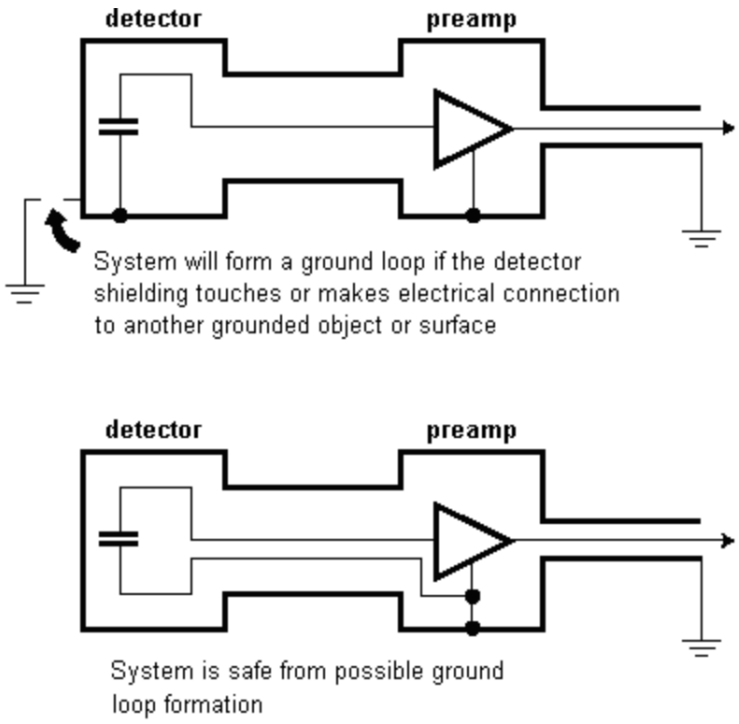

Figure 5.2: Schematic of incorrect and correct connection of shielding [17].

5.1.3 Cooling

To reduce thermal noise and achieve better SNR, it is necessary to cool the detector. Cooling can be achieved in a number of ways. In most setups, a Peltier cooler can provide the appropriate solution. These Peltier setups are the easiest to implement, but their cooling efficiency is highly dependent on the ability to sink the heat from the hot side.

5.2 Spectrometric chain components

5.2.1 Pre-amplification

The signal coming from the PIN detector is a charge (current pulse), so it is necessary to convert it into a voltage pulse. To perform the charge-voltage conversion, there is a circuit called a charge amplifier (also called a preamplifier). The main functional scheme is described by an opamp with a capacitor in feedback (see figure 5.3). The functionality is similar to an I/U transimpedance amplifier, but the charge amplifier works mainly as an integrator. In the ideal case (opamp gain $G >> 0$) the measured voltage per unit charge is approximately equal to:

$$\frac{dU}{dQ} = \frac{1}{C_f}. \tag{5.1}$$

In a real circuit there is also a resistor in parallel with the feedback capacitor. The feedback resistor slowly discharges the capacitor after an accumulation of charge, making the transimpedance amplifier ready to capture another pulse. The output voltage has an exponential decay shape with amplitude defined by the energy deposited in the detector, a short rise time (in the order of nanoseconds) and a longer decay constant (microseconds). Since the output of the preamplifier is in the order of millivolts, it must be highly amplified. A very fast and low-noise amplifier consisting of several opamps is a suitable solution to this problem. Charge preamplifiers are also very sensitive devices and can be easily damaged by electrostatic charges.

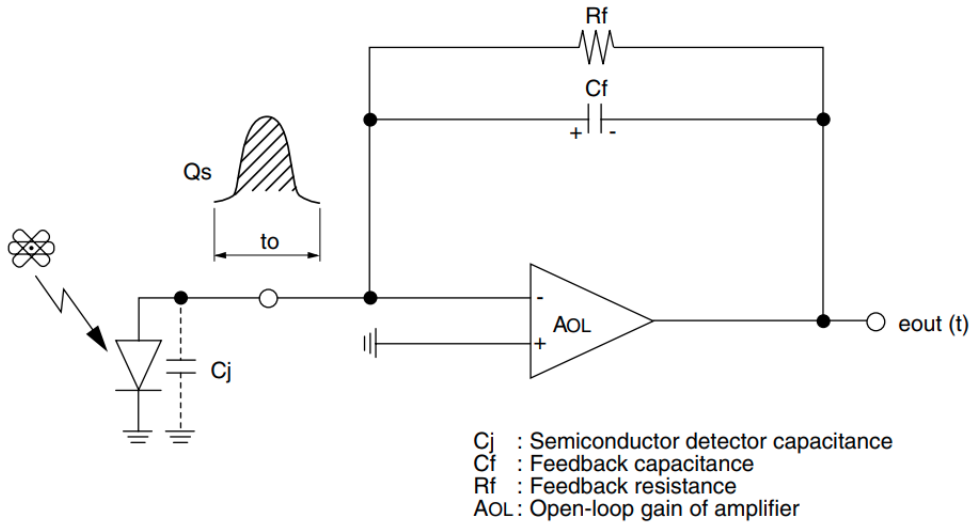

Figure 5.3: Charge ampifier. Qs is total charge of pulse and to is the interval of charge generation inside the detector. Taken from [18].

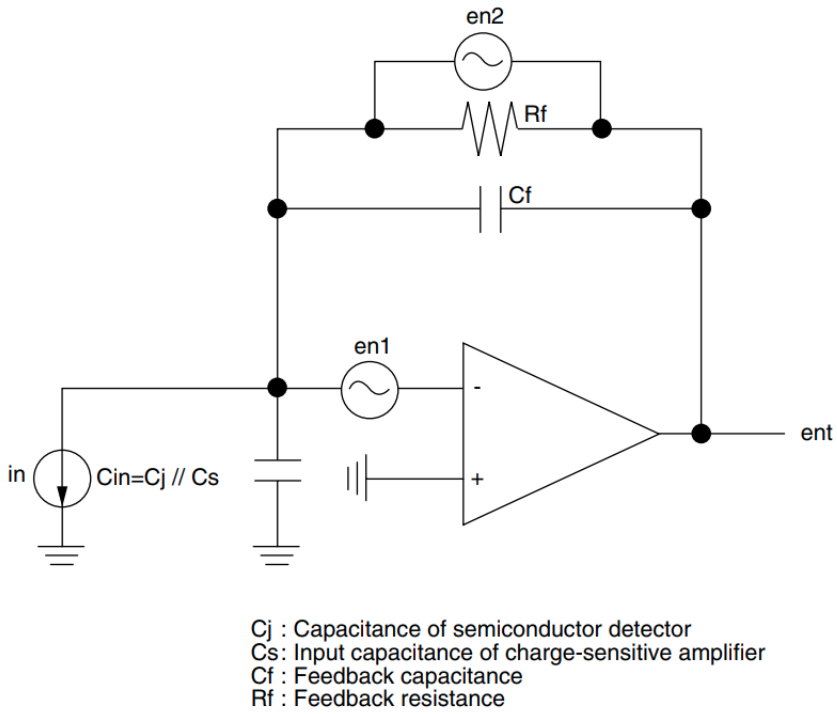

Figure 5.4: Noise equivalent circuit for charge amplifier. Taken from [18].

The functionality of the charge amplifier is also negatively affected by electronic noise, which depends on the values of the feedback resistance and capacitance, as well as on the internal parameters of the connected semiconductor detector and the field effect transistor (FET) inside the amplifier. The noise model of the preamplifier circuit is shown in the figure 5.4. This electronic noise can be divided into three contributions, each described by equations for noise voltages and currents [18]:

- Thermal noise of the first stage FET:

$$en_1 = \sqrt{\frac{8}{3}\frac{kT}{g_\mathrm{m}}}, \tag{5.2}$$

  where k is the Boltzmann constant, T is the absolute temperature and g_m is the transconductance of the FET.

- Shot noise caused by FET gate current and detector dark current:

$$in = \sqrt{2e(I_\mathrm{G} + I_\mathrm{D})}, \tag{5.3}$$

  where e is the elementary charge, I_G is the gate leakage current of the first stage FET and I_D is the dark current of the detector.

- Thermal noise caused by feedback resistance:

$$en_2 = \sqrt{4kTR_\mathrm{f}}, \tag{5.4}$$

  where R_f is the feedback resistance.

The square of total noise $ent^2(j\omega)$ is given by equation:

$$ent^2(j\omega) = en_1^2 \cdot (1 + \frac{C_{\text{in}}}{C_{\text{f}}})^2 + \{in^2 + (\frac{en_2}{R_{\text{f}}})^2\} \frac{1}{(j\omega C_{\text{f}})^2}, \tag{5.5}$$

where C_{f} is the feedback capacitance, C_{in} is the resulting capacitance at the amplifier input (there - parallel combination of the detector capacitance C_{j} and the amplifier input capacitance C_{s}), ω is the angular frequency and j is the complex unit.

The first term in the equation 5.5 depends on the ratio between the input capacitance C_{in} and the feedback capacitance C_{f}, so the feedback capacitance of the preamplifier must be optimised to reduce the electronic noise.

For the PCB design we used a CR-110-R2 charge amplifier from Cremat Inc. This preamplifier also contains the second stage - the common voltage amplifier. CR-110-R2 offers the conversion gain $G = 1.4$ V/pC, decay constant $\tau = 140$ μs CR-110-R2) and noise (FWHM) in silicon equal to 1.7 keV [19]. It can be easily calculated that for a 14.4 keV photon, the output pulse has an amplitude equal to $U_A = 0.8928$ mV. Note that the noise introduced by the preamplifier is much larger than the intrinsic Fano noise ($\text{FWHM}_{\text{Fano}} = 185.4$ eV). Its internal scheme can be seen in the figure 5.5.

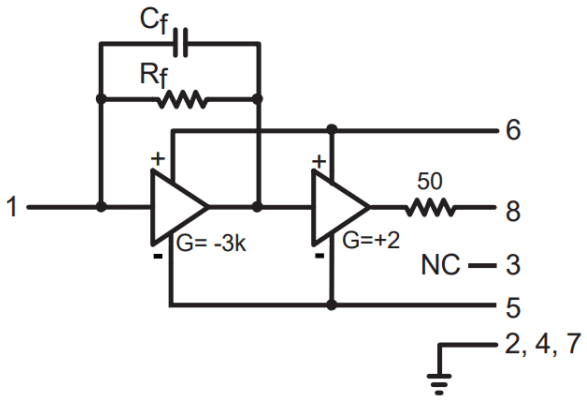

Figure 5.5: Internal scheme of CR-110-R2 charge sensitive preamplifier [19].

The modular version suitable for our application is the ORTEC 142A charge preamplifier with $G = 1.016$ V/pC, $\tau = 500$ μs and noise in silicon equal to 1.6 keV [20].

5.2.2 Shaping

To perform accurate energy discrimination, the pulse shape must be changed from an exponential decay shape by a shaping circuit. Shaping results in filtering the frequency band (reducing noise) and also shortens the long decay times of the original exponential shapes. The shorter duration of the pulses prevents the negative effect of one pulse being superimposed on another one (pile-up effect).

The Gaussian shape satisfies the optimum parameters of SNR and duration [21]. This type of shaping is usually achieved by several integration stages. The Cremat module CR-200-1us-R2.1 offers Gaussian shaping with a shaping time of 1 μs [22]. Its simplified internal schematic is shown in the figure 5.6.

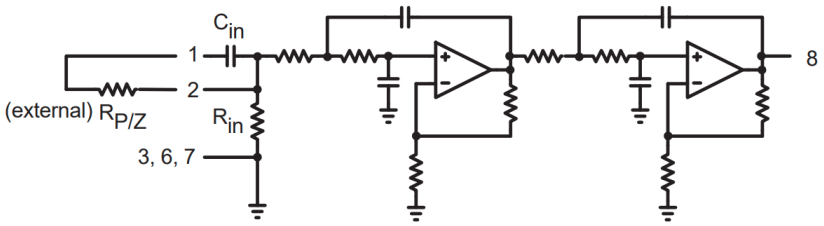

Figure 5.6: Internal scheme of CR-200 Gaussian shaping amplifier [22].

The shapers are usually very sensitive to the shape of the input pulse. They expect a step-like input pulse. The deviation from the expected shape can result in an undefined shape at the output of the shaper.

5.2.3 Multichannel analysis (MCA)

To obtain full energy spectrum information, it is necessary to measure and digitise the pulse height of the incoming pulses to perform energy discrimination and increment the corresponding channels. The multichannel analyser (MCA) can be used for this purpose. The EASY-MCA-2K from ORTEC [23], which we are using in the experiments, is capable of processing Gaussian shaped pulses with shaping times from 0.25 μs to 30 μs and amplitudes from 0 to +10 V.

Chapter 6

Gamma spectrum software analysis

As mentioned in section 1.2.2, the measured gamma spectrum contains many unwanted artefacts such as noise, Compton continuum and edges, and additional peaks caused by various interactions. To correctly obtain the count rates at defined energies, it is necessary to perform a numerical analysis of the measured data. Locations of energy peaks are found, for example, by their characteristic second derivatives. Absolute count rates are then obtained by Gaussian fitting.

6.1 Peak searching procedure

Many commercial programs use peak search procedures based on an algorithm originally developed by M.A. Mariscotti [24]. This method is based on the numerical second difference, which assumes that the background can only be approximated by linear functions and therefore vanishes in the second derivative. The second fact is that the searched peaks are Gaussians with their specific second derivatives and thus their positions can be found in local minima (Gaussians have negative second derivatives as they are concave functions). To reduce noise, the second difference is averaged over a defined number of steps. Rules based on the value of the standard deviation of the second difference at a given point and other additional rules based on the number of points in specified intervals can be used to determine whether the found minimum should be considered as a peak position (and not as a Compton edge, etc.). However, the algorithm requires input parameters based on a raw estimation of the FWHM of the searched peaks.

For the analysis of measured gamma spectra, this algorithm was implemented in C++ and used to find peaks and edges. The following figures 6.1 and 6.2 show the example of measured spectra and their second difference plotted together with their calculated standard deviation. The possible candidates for peak positions can be observed.

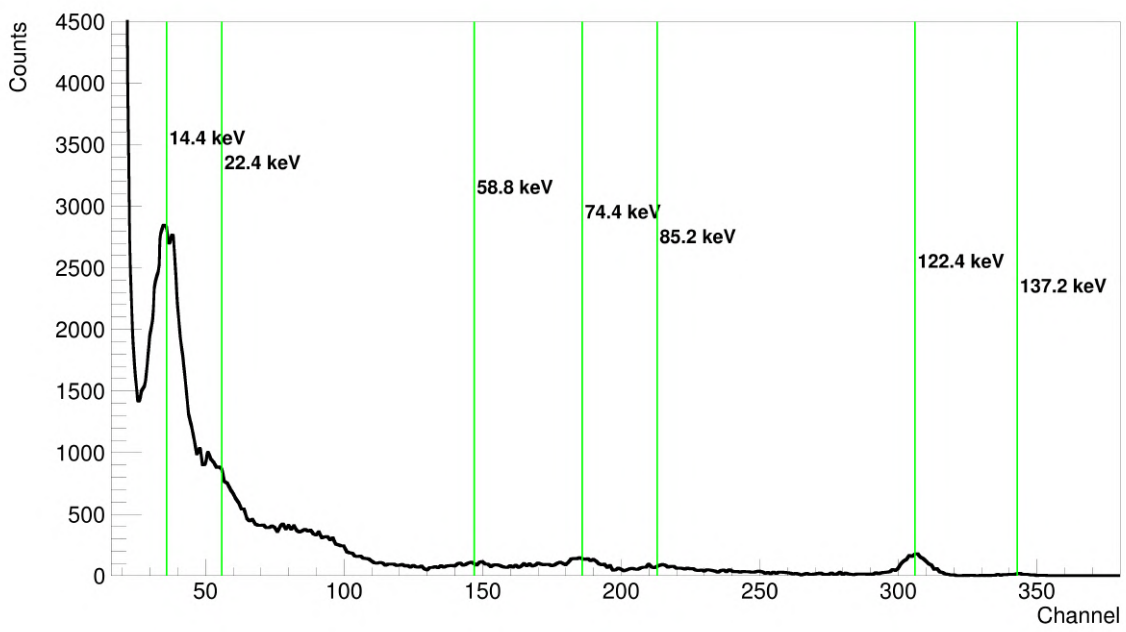

Figure 6.1: Example of measured gamma spectra. Green lines mark the energy peaks found by algorithm.

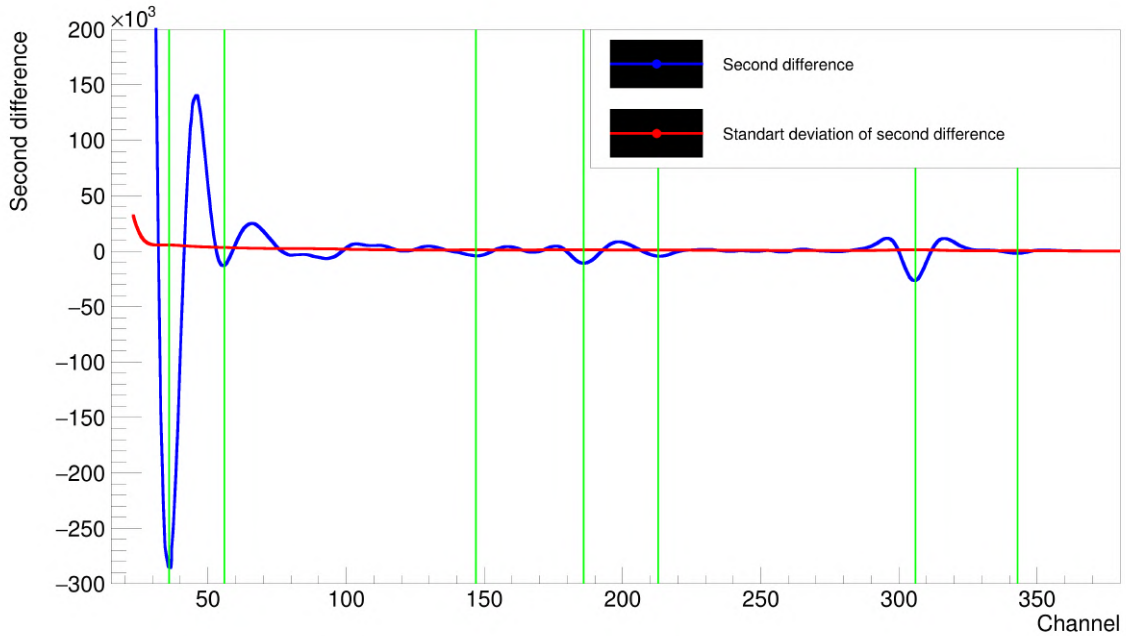

Figure 6.2: Second difference of example spectra along with its standard deviation showing possible candidates (green lines).

Chapter 7

Gamma detection testing

The purpose of this experiment is to determine the conditions necessary for selected photodiodes to be used as detectors for gamma spectroscopy. Note that some of the selected photodiodes are not intended to be used as gamma-ray detectors. The determination of the detection efficiency will be precisely done in the following chapters.

For the very first test of the photodiodes, we assembled a spectrometric setup consisting of ORTEC modules including a preamplifier ORTEC142A, a shaping amplifier 575A and a high voltage power supply 556 inside the ORTEC minibin (figure 7.1). The pulses were captured by ORTEC's EASY-MCA-2K connected to a PC running the MAESTRO Multichannel Analyzer Emulation Software [25]. As radioactive source we used ^{57}Co 50 mCi Mössbauer source (date of production: 3.11. 2016) and therefore it was also necessary to cover the part with radiation source with lead shielding blocks.

Figure 7.1: ORTEC minibin with Easy MCA connected to PC.

7.1 Noise reduction

When performing gamma spectroscopy measurements, the energy spectra are affected by noise. To reduce the noise as much as possible, two approaches have been tested - shielding the detector in various ways and cooling it.

7.1.1 Electromagnetic noise reduction

Photodiodes must be adequately shielded from electromagnetic interference and their distance from the preamplifier input should be as short as possible. The use of poorly shielded diodes leads to high levels of electromagnetic noise, which makes a large part of the energy spectrum unobservable.

Based on many tests, it has been proven that the optimal way to shield the photodiode is to place it in an aluminium box (see figure 7.2). This crate must be as small as possible and connected to the ground potential. However, the front of the crate must be open to allow sufficient transmission of gamma photons to the detector. To preserve the shielding properties, this hole has to be covered with a conductive material. We chose a thin aluminium foil, which has sufficient gamma transmission parameters as well as electromagnetic shielding parameters.

Figure 7.2: Photodiodes inside aluminium shielding crates.

7.1.2 Thermal noise reduction

To reduce thermal noise, the S14605 photodiode was cooled with ice. It was placed in a shielding box with a heat sink attached to the bottom. This heat sink was submerged in the small tub filled with ice (see figure 7.3). Thermal conduction was improved by sticking the photodiode to the bottom of the shielding box with thermal paste. The photodiode was cooled in this way to temperatures around 7-8 °C.

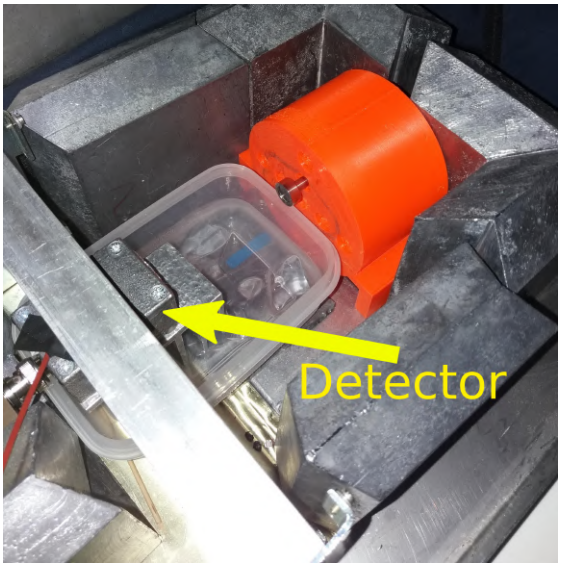

Figure 7.3: Detector cooled by ice.

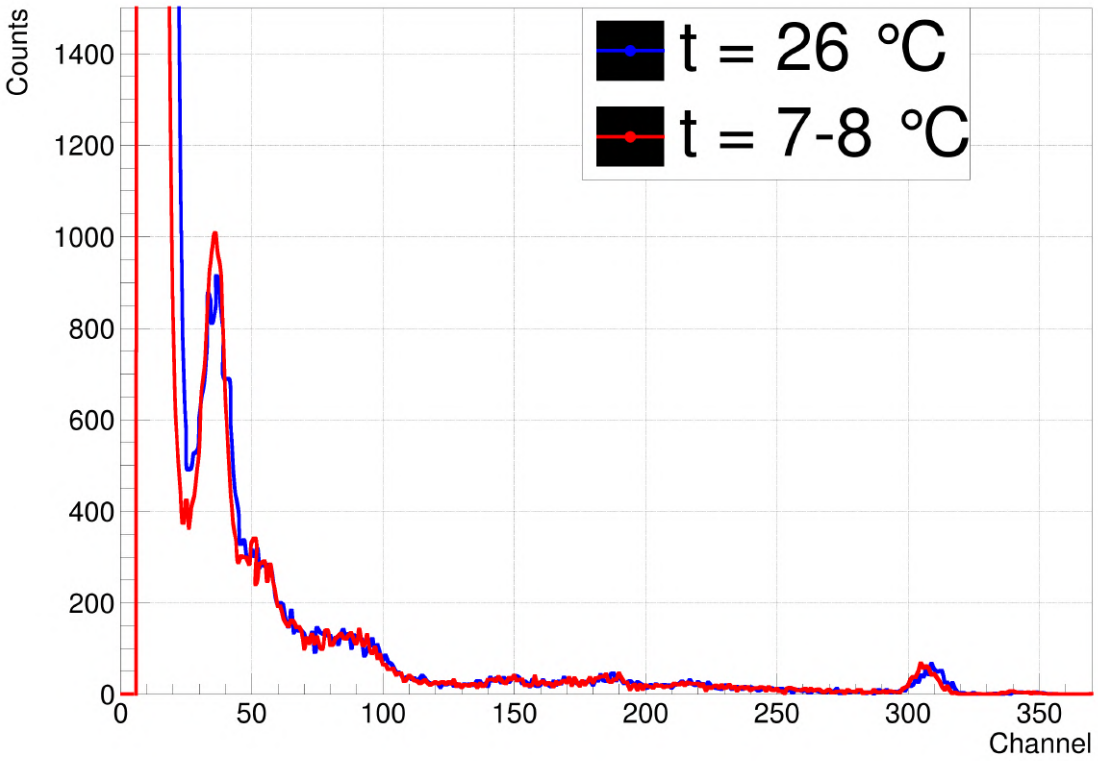

Figure 7.4: Measured ^{57}Co spectra at two different temperatures.

The results show that cooling improves SNR, but its effect is small compared to the effect of proper shielding. The cooling is not used in the following tests on the ORTEC setup.

7.2 Test measurement of the ^{57}Co spectra

The spectra for each photodiode were acquired for 30 min of live time - MCA allows dead time compensation which extends the total real time of the spectrum acquisition. The source was placed at a distance of 1 cm from the front shielding box (figure 7.5) and to recognise the corresponding peaks, the set of the following filters was placed between the source and the detector:

- Pb filter: everything should be attenuated.
- Cu filter: transmitted - 122.1 keV, 136.5 keV absorbed - 14.4 keV, 6.4 keV.
- Al filter: transmitted - 122.1 keV, 136.5 keV, 14.4 keV absorbed - 6.4 keV.

Figure 7.5: Setup for ^{57}Co gamma spectrum measurement with filters. PIN photodiode is situated inside the shielding crate, which is connected to the preamplifier.

The spectrum is analysed using our own peak finder program (described in section 6.1) to find the characteristic energy components. The 14.4 keV channel position is then used to calibrate the energy axis of the MCA spectrum. The Compton edge caused by the interaction of 122.1 keV photons inside the detector can be expected. The equation 1.8 predicts the position to be around 39.5 keV.

7.2.1 S14605 test

The optimal bias voltage of 50 V has been determined experimentally - any further increase does not improve the noise. The measured spectra with no filter, with special filters and only background (fully shielded) are shown in the figure 7.6.

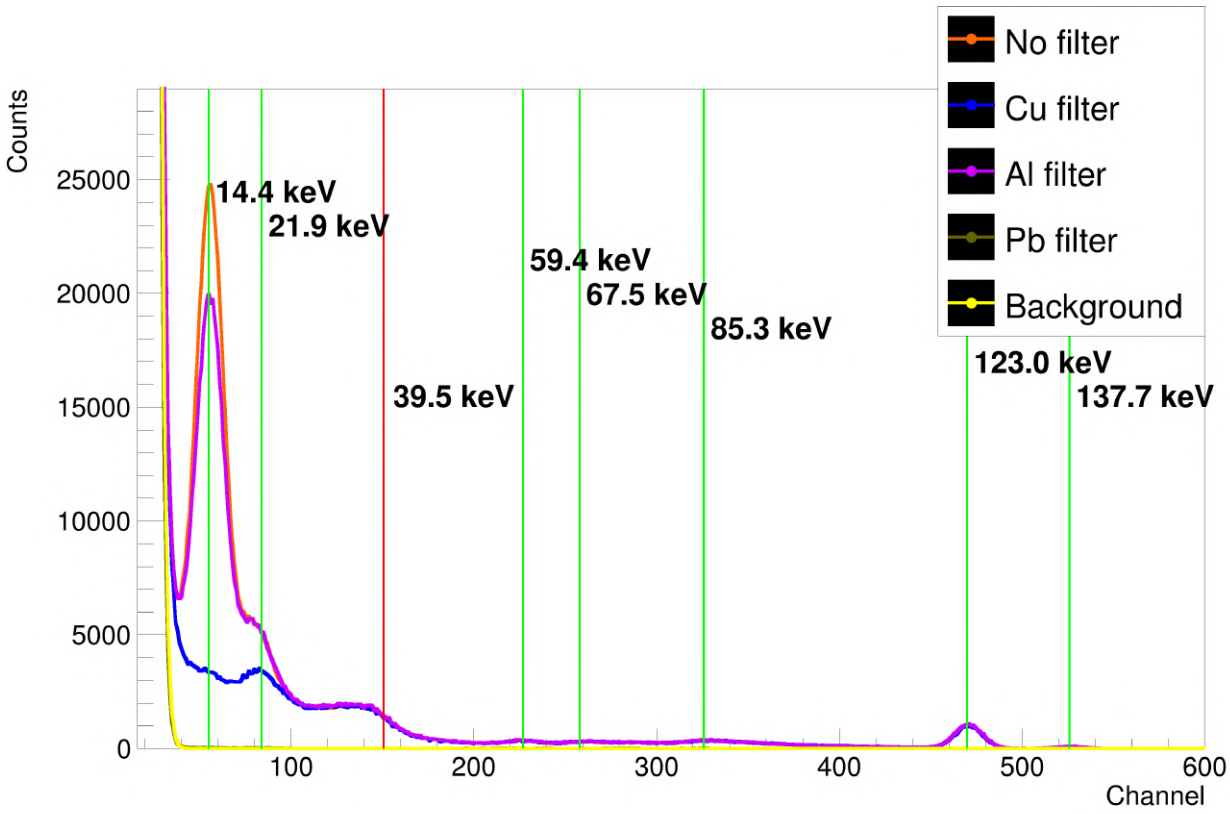

Figure 7.6: S14605 spectra with founded energy peaks (green lines) and predicted Compton edge (red line).

The first peak was determined to be a 14.4 full energy peak as it is absorbed by the Cu filter. The 21.9 keV peak is from characteristic X-rays of the rhodium matrix, and 59.4 keV may also originate from the source matrix. The 67.5 keV and 85.3 keV peaks are most likely characteristic X-rays from the lead shielding. The last two peaks (123.0 keV, 137.7 keV) are from ^{57}Co. It can be seen that the detection efficiency of the full energy at higher energies (122.1 keV) is very low, and that Compton scattering is preferred interaction effect inside the detector at these energies, resulting in the expected Compton edge. The expected peak at 6.4 keV is hidden in the electronic noise.

7.2.2 BPW34 test

The instrumentation was similar to before, but BPW34 had to be operated at a lower bias voltage, so 20 V was chosen as the optimum. The measured spectra are shown in the figure 7.7.

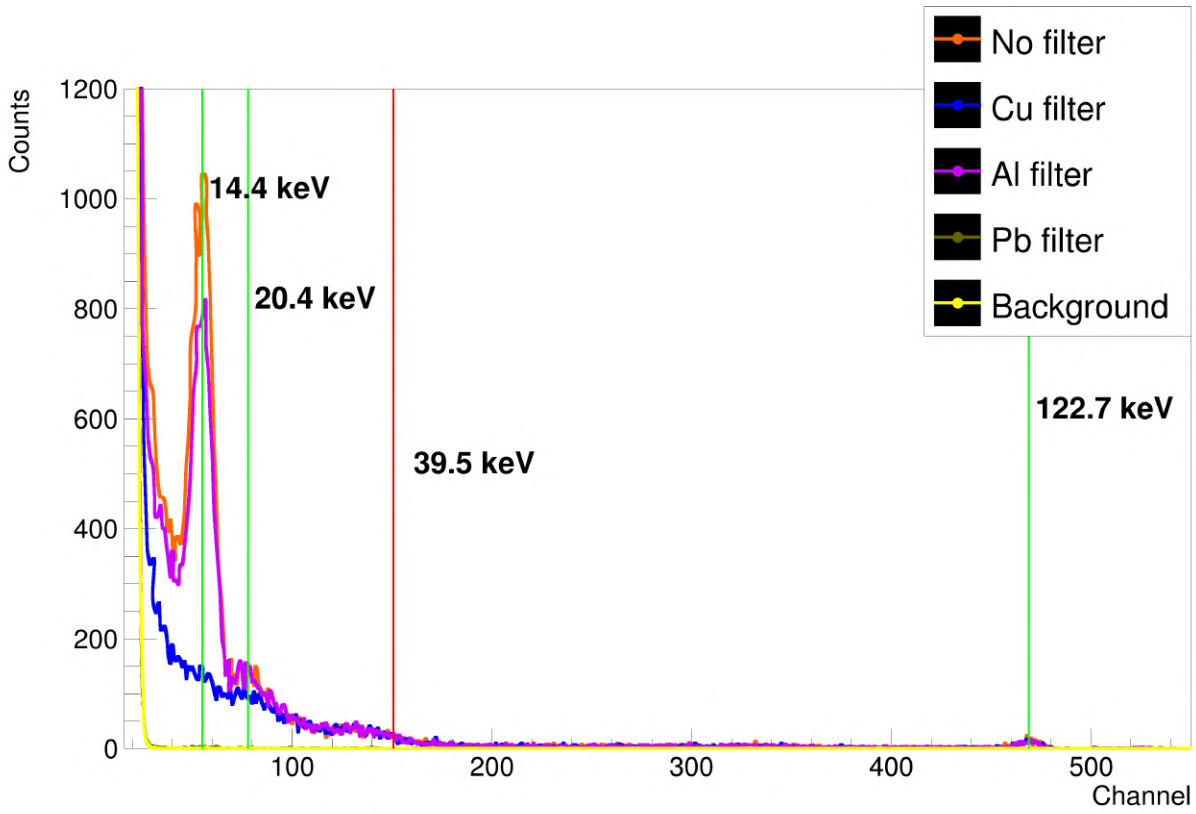

Figure 7.7: BPW34 spectra with founded energy peaks (green lines) and predicted Compton edge (red line).

The measured spectra of BPW34 are very similar to the previous one, but the peak heights are about 25 times lower. The results also confirm the fact that the Si semiconductor structure with p-n or p-i-n junction detects the gamma photons with the same signal strength without any dependence on the dimensions. Only the detection efficiency depends on the dimensions.

7.2.3 OPF430 test

The OPF430 was operated at 20 V. There was a problem with the very low detection efficiency, so the source had to be placed in the shielding box just before the photodiode. Spectra acquired in this way are shown in the figure 7.8.

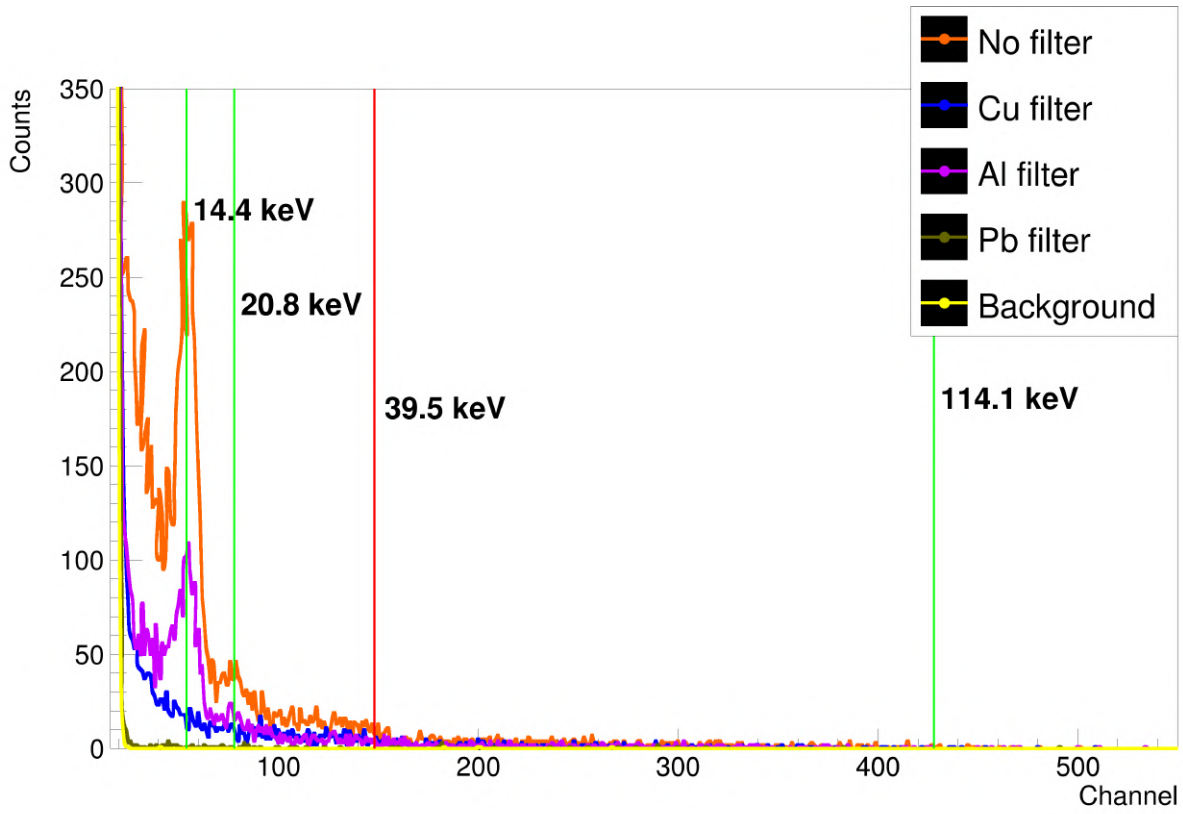

Figure 7.8: OPF430 spectra with founded energy peaks (green lines) and predicted Compton edge (red line).

It can be seen that the count rates are still much lower compared to previous photodiodes. This is probably due to the fact that the detector area is very small. The conclusion is that the OPF430 is capable of capturing the low energy gamma rays, but the efficiency is so bad that it is unusable for any real gamma spectroscopy application.

Chapter 8

Design of integrated amplifier

The only way to improve the performance of the spectrometric chain is to integrate the preamplifier, amplifier and a shaper on a small PCB, as the ORTEC setup does not allow any upgrades. This includes shortening the signal paths, reducing the parasitic capacitance at the preamplifier input and improving the shielding. The various prototypes were designed as double-sided PCBs and manufactured using a milling machine. The PCB, consisting mainly of surface mount deposition (SMD) components, was then assembled by manual soldering.

8.1 Electronic schematic and layout

The main parts of the integrated amplifier are: photodiode input connector, preamplifier, second stage amplifier, shaper module, output buffer optimised for 50 Ω transmission line, bipolar voltage supply for modules and bias voltage supply for photodiode. To surround the sensitive parts with sufficient shielding, the PCB is placed in an aluminium box with a window drilled for the photodiode (figures 8.1 and 8.2). The complete schematic and layout of the integrated amplifier can be found in appendix.

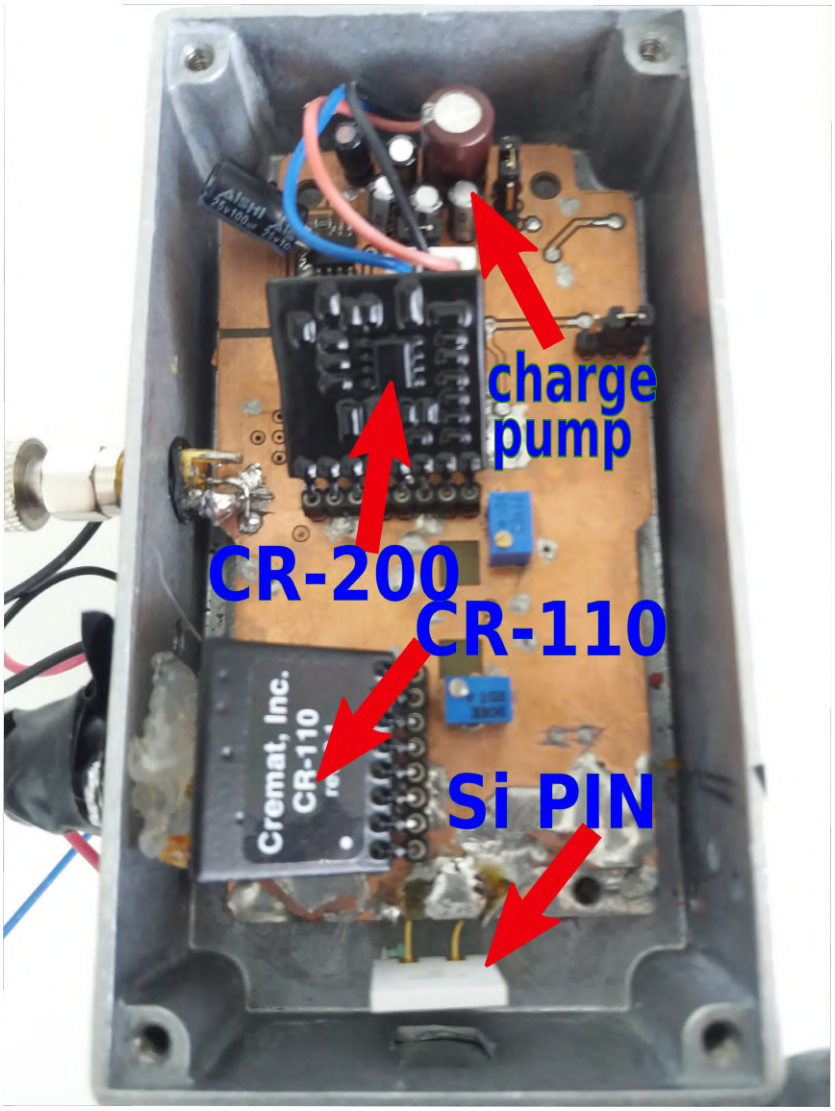

Figure 8.1: Fully assembled integrated amplifier PCB with attached Cremat modules inside the shielding box.

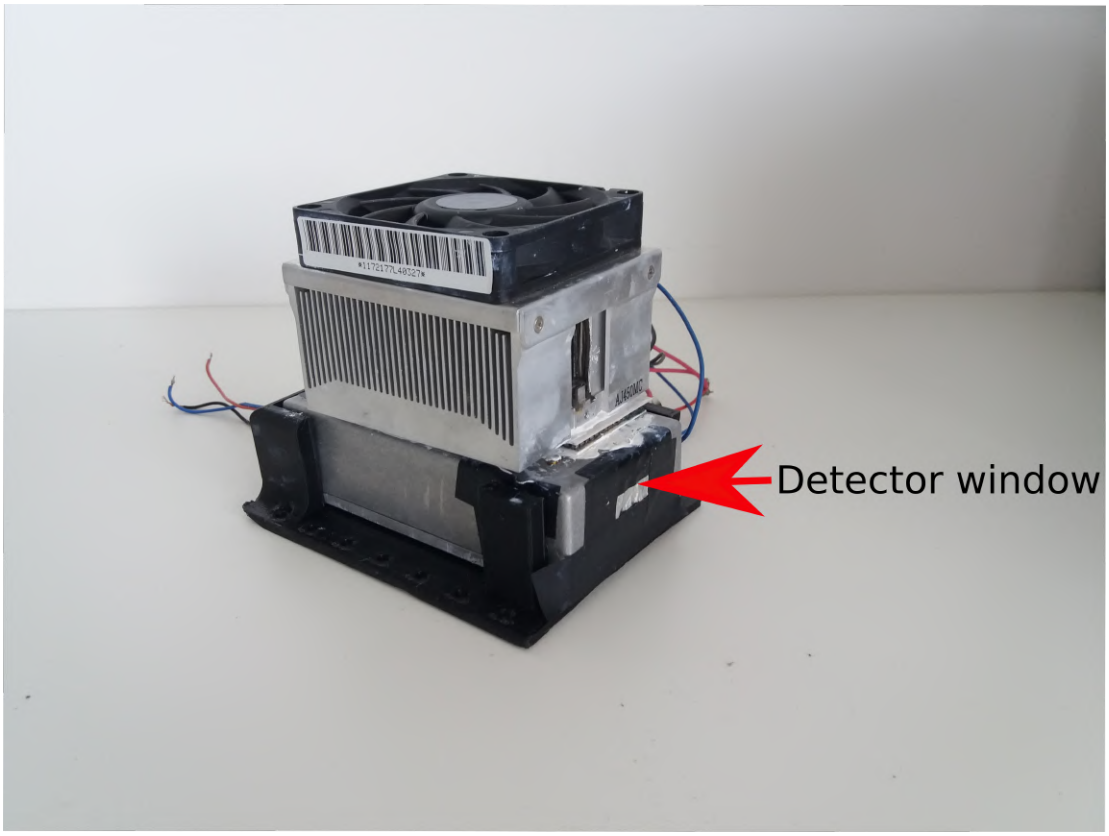

Figure 8.2: PCB in aluminium box with attached peltier coolers.

8.2 Grounding and shielding

To ensure that all currents have their return path with sufficient conductivity, the main GND signal must be spilled all over the board. Even a small amount of resistance in these paths can cause disturbing voltage dropouts. Currents from non-signal parts, such as the charge pump, should have a different return path from the signal parts, so the spilled GND must be split into two separate parts (signal and bias supply) that are connected only at the input voltage connector. This type of layout is referred to as a star ground structure [27].

The shielding box must be connected to GND in a specific location to prevent the induced currents from the shielding to flow through the signal ground of the detector. The best location to connect the shielding box to GND is near the voltage supply connector.

8.3 Photodiode input and preamplifier

The photodiode is inside the box and the cathode is connected to the bias voltage and the preamplifier (CR-110) by capacitive coupling (10 nF capacitor). The CR-110 application note also mentions an optional 220 Ω resistor to be connected before the coupling capacitor to prevent the CR-110 from being damaged by large current spikes. Our experience shows that this resistor should not be omitted. The signal path from the photodiode to the preamplifier input should be as short as possible.

8.4 Amplification and shaping

The preamplifier output is routed to the amplification stages via capacitive coupling (to eliminate unwanted offset) and potentiometer dividers (to adjust signal amplitude). First amplification is achieved by two non-inverting amplifiers with OPA847 op-amps. Each stage has a gain of 22×. Additional gain of 10× is provided by the CR-200 shaper module. The OPA847 opamp datasheet [28] describes that these fast opamps are prone to unwanted oscillations due to the parasitic capacitances between input, output and supply, and therefore the GND around the opamp must be removed from both sides of the PCB. The output of the shaper module is routed directly to the MAX4201 output buffer opamp, whose output is connected to the output SMA connector mounted on the aluminium box.

8.5 Voltage supply

The power supply (typically +15 V and -15 V) is adjusted using LM317 and LM337 regulators, which convert the input supply voltages to +7 V and −4 V. However, these regulators generate heat, which has a negative effect on SNR, so this heat has to be taken out of the PCB by the thermal bridge connection to the aluminium box. To stabilise the temperature during long runs, the shielding case has two additional Peltier couples with fan attached.

The S14605 requires a bias voltage of around +50 V, which is supplied by a 3-stage charge pump, simply assembled from capacitors, diodes and a PWM generator - NE555. The charge pump is theoretically designed to multiply the input voltage from +15 V to +60 V. However, due to the fact that the rectifying diodes have some dropout, and also because the charge pump is not a stiff voltage source (even small currents in the order of mA cause large dropout), the real bias voltage is around +50 V. The pump's output needs to be filtered, as it can contain voltage spikes from the switching frequency (10 kHz). To filter this high voltage output, the high voltage opamp OPA454 is connected as a buffer - the pump voltage is connected as the opamp supply, and the voltage from the regulator (+7 V) is connected to the negative input pin of the opamp. There is also a jumper to select between +15 V and +50 V for both the SI14605 and BPW34 PIN.

Chapter 9

^{57}Co MCA measurement with integrated amplifier

In order to properly test the assembled integrated amplifier with attached S14605 photodiode (hereafter referred to as Si PIN detector) and to compare its detection efficiency for 14.4 keV photons with the detection efficiency of the other types of detectors - scintillator and gas detectors - the measurement setup was constructed with a carefully designed geometry.

The on-board gain is set to observe the 14.4 keV energy peak in the second half of the channel range, which on the other hand means that the photons of higher energies cannot be observed as they are in saturation, but the detection of these energies is not our focus.

For each detector the sequence of five measurements was performed - without filter, with three filters and without source. The relative detection efficiency for 14.4 keV is determined by a Gaussian fit of the 14.4 keV peak in spectra with background subtracted. Each spectrum measurement was performed with 1200 s of live time, i.e. with compensation for dead time.

9.1 Measurement setup

The measurement setup consists of 3D printed parts - plastic holders for each detector and holders for radiation filters. All the holders have to be modular and easily interchangeable to keep the geometry the same for each detector. The 50 mCi ^{57}Co source (date of production: 12.10. 2020) is mounted on the transducer (switched off for this measurement). To compare the detection efficiency of detectors with different detection areas, the irradiation has to be done through a collimator, so the detector is irradiated through a hole ($d = 4$ mm) in a lead shielding.

The detector output is connected directly to the ORTEC MCA. For peak identification three filters were placed in front of the lead collimator - Cu (255 μm), Al (780 μm), Pb (5 mm).

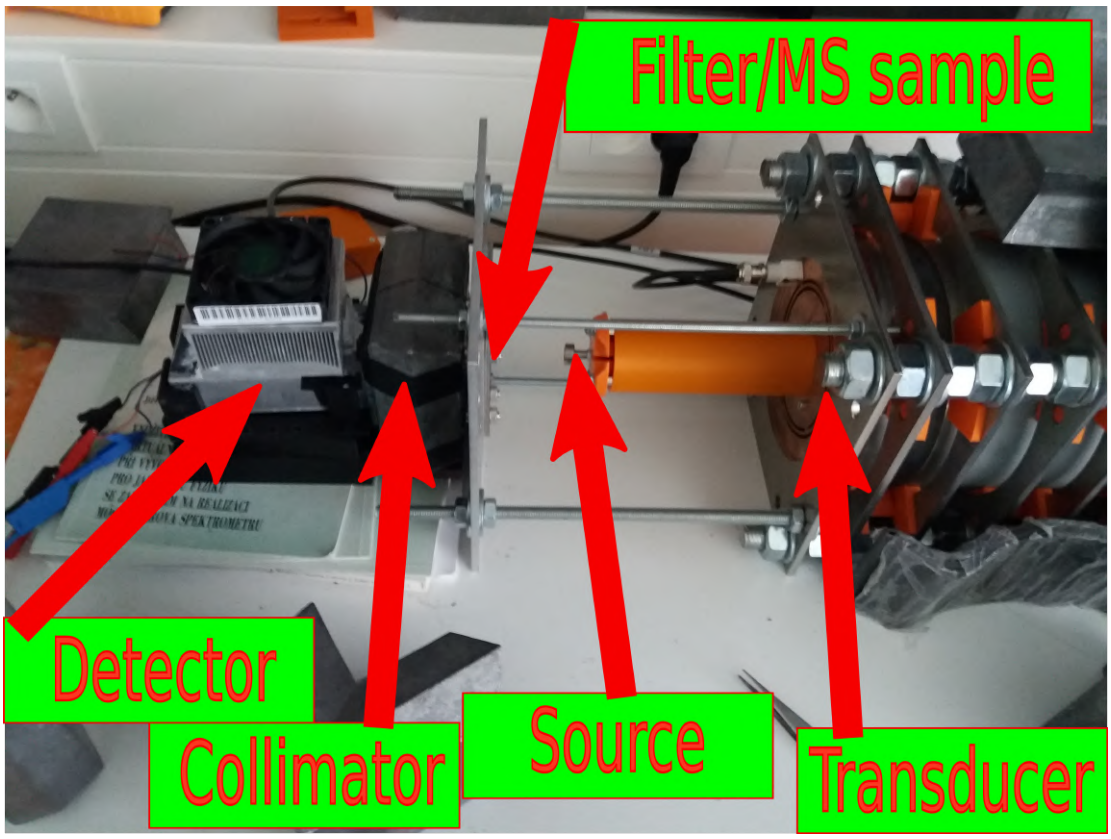

Figure 9.1: Measurement setup for MCA/MS.

9.2 Si PIN detector measurement

The measurement with the Si PIN detector was performed using the previously specified setup. The measured spectra are shown in the figure 9.2.

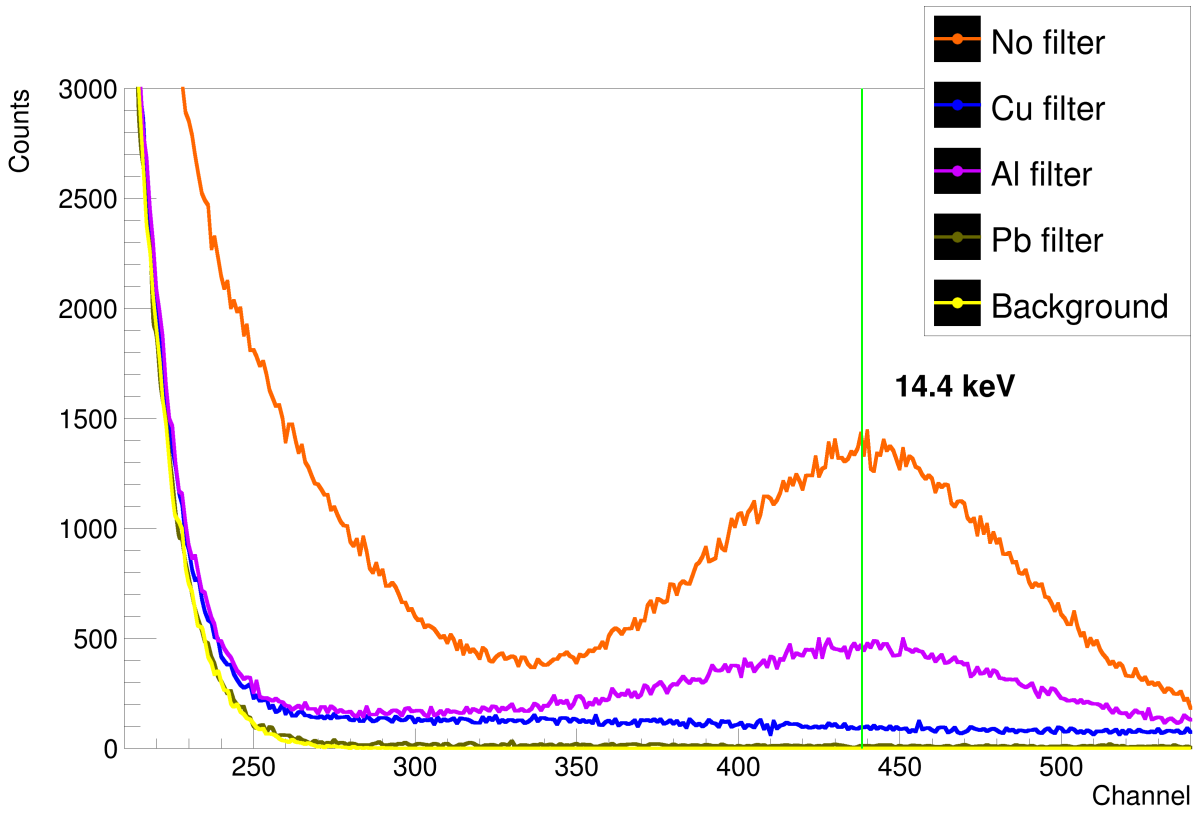

Figure 9.2: Si PIN detector ^{57}Co spectra.

It can be seen that the noise in the spectrum is much lower than in the case of the ORTEC setups. The part of the 6.4 keV peak can also be seen. Several ways have been tried to reduce the noise - cooling with ice, improving the shielding, etc. However, none of them resulted in the peak of 6.4 keV energy without noise. The main part of the remaining noise probably comes from the Si PIN diode capacitance ($C_{\mathrm{S14605}} \approx 25$ pF). This was confirmed by using the same PCB with a photodiode of smaller capacitance (e.g. BPW34, $C_{\mathrm{BPW34}} \approx 10$ pF). Spectra of the BPW34 connected to the integrated amplifier can be seen in the figure 9.3. The FWHM of the 14.4 keV peak is $\mathrm{FWHM}_{14.4}$ = (3.62 ± 0.06) keV. When this value is compared to the limit given by preamplifier CR-110 ($\mathrm{FWHM}_{\mathrm{CR\text{-}100}} = 1.7$ keV) we come to the conclusion, that there is still a room for improvement of the following amplification stages.

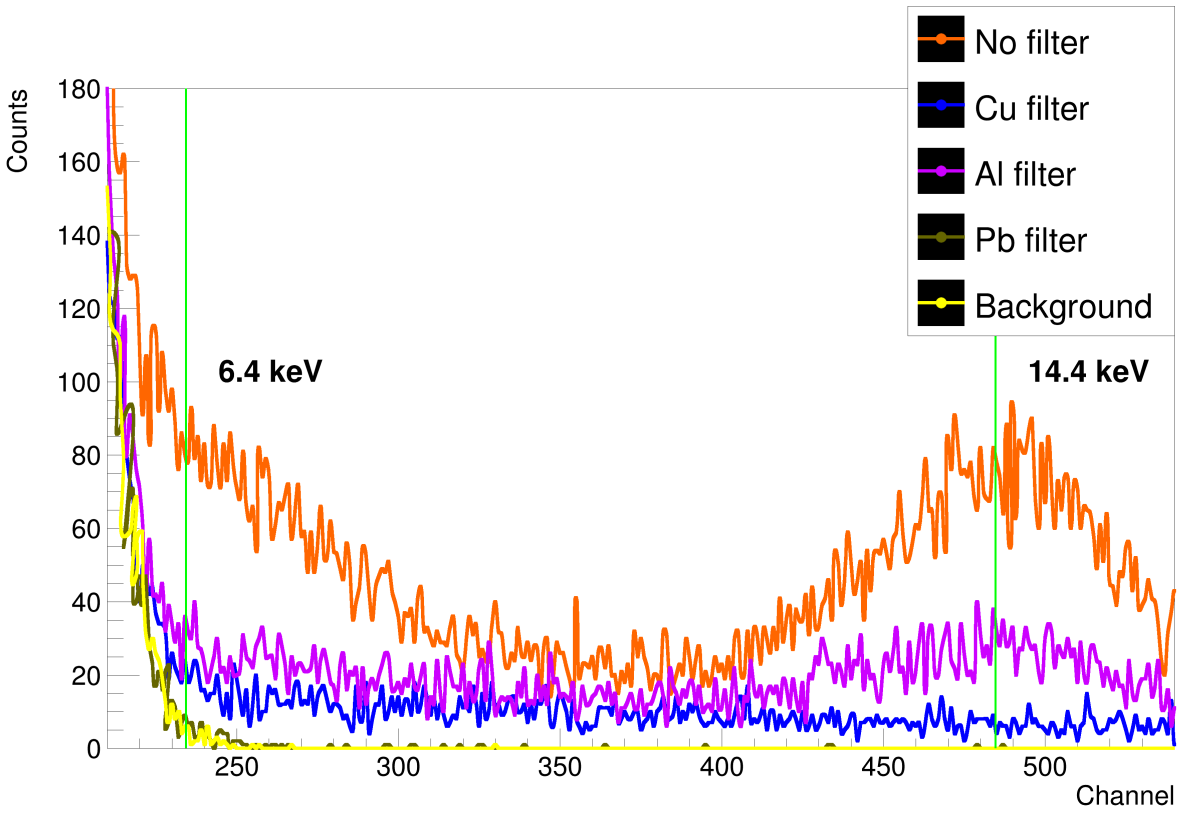

Figure 9.3: Spectra of BPW34 attached to the integrated amplifier.

9.3 Scintillator and gas detector measurement

The same setup was used to measure the relative efficiency of the scintillator and the gas detector. For the gas detector, the LND45479 tube was used, optimised for 14.4 keV detection with amplification electronics also based on Cremat modules. For the scintillator detector, we chose the R6095 photomultiplier tube [29] with a C9028-01 socket [30]. The scintillator crystal used is YAP(Ce) with a thickness of 0.4 mm and the amplification is done by a custom built amplifier [16]. The measured spectra for the scintillator are shown in the figure 9.4 and for the gas in the figure 9.5.

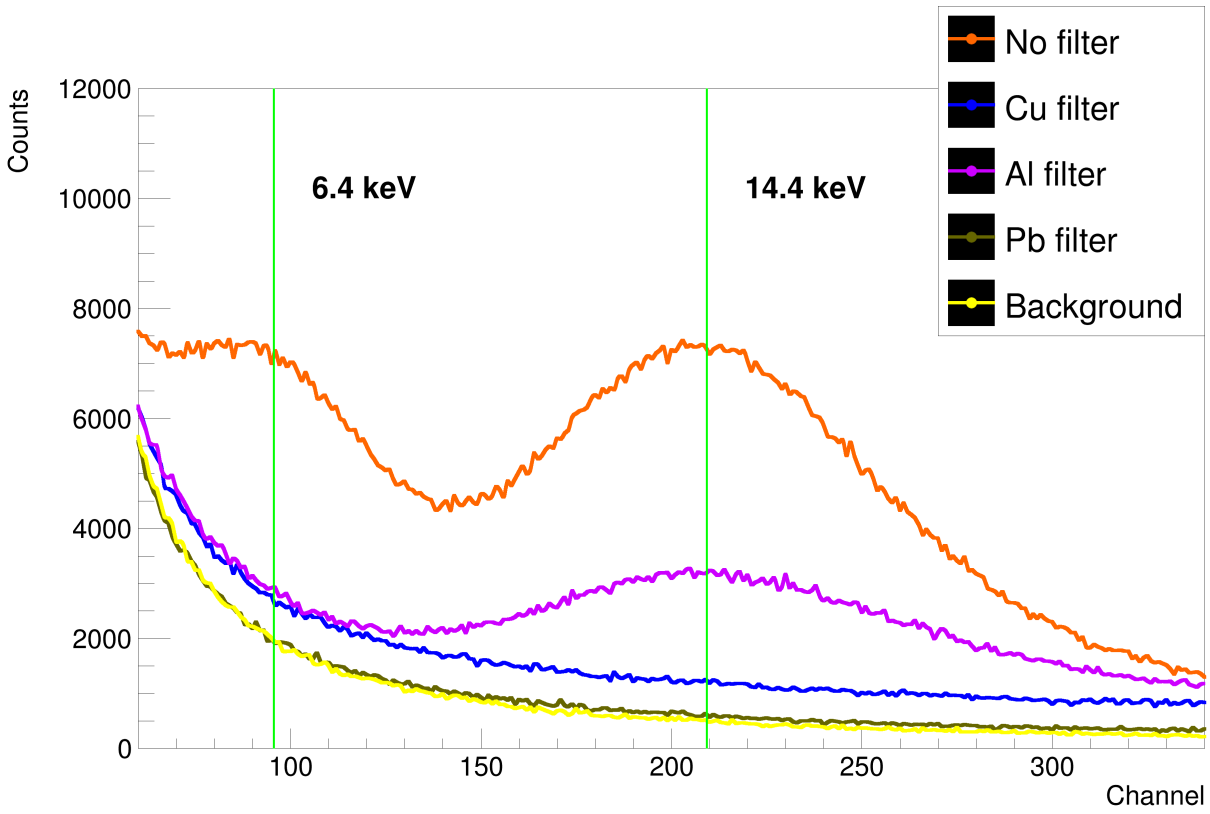

Figure 9.4: Scintillator ^{57}Co spectra.

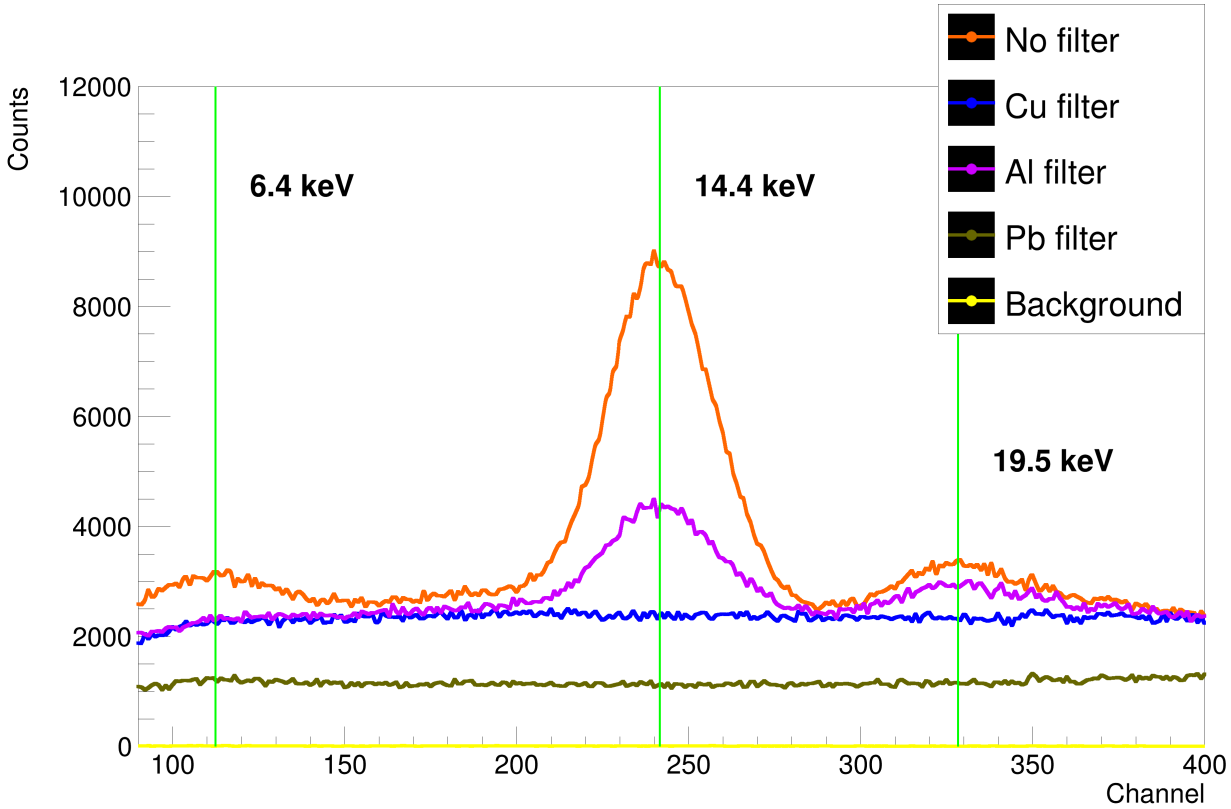

Figure 9.5: Gas ^{57}Co spectra.

In the spectra of the gas detector, three narrow peaks can be observed - a 14.4 keV

peak and two small peaks - 6.4 keV and 19.5 keV. It also has a high level of Compton continuum. The scintillator sees both the 6.4 keV and 14.4 keV full energy peaks. However, its energy resolution is much worse - both peaks are significantly broader and overlap each other.

9.4 Results

The sum of the total counts for the 14.4 keV and 6.4 keV full energy peaks and the relative detection efficiency with respect to the most effective detector were calculated as follows:

1. The spectra with the Cu filter are subtracted from the spectra without the filter. This provides sufficient suppression of the Compton continuum caused by 122.1 keV photons.

2. The spectra obtained in the previous step are fitted by a sum of Gaussians. The spectra of the Si PIN and the scintillator were fitted by the sum of 2 Gaussians, and in the case of the gas the sum of 3 Gaussians is used due to the wider channel interval.

3. The value of the absolute counts (area under the Gaussian) for the given energy spectra is calculated from the fit parameters with the uncertainties also taken from the fit.

	absolute	relative
Si PIN	143000 ± 3000	0.291 ± 0.008
gas	231000 ± 2000	0.48 ± 0.01
scintillator	491000 ± 9000	1

Table 9.1: Table of calculated absolute and relative counts of 14.4 keV photons for each detector.

The peak of 6.4 keV photons is not fully observable in the case of the Si PIN detector. However, a rough estimate can be calculated using parameters obtained from a Gaussian fit of the partial 6.4 keV peak. The results in table 9.2 should be considered as indicative only. Note also that the setup wasn't designed to detect 6.4 keV photons - some detectors have slices of Al coating in the detector window (Si PIN - 1× 7 μm thick aluminium foil, scintillator - 3× 7 μm thick Al foil, gas - window of unknown metal). A thick aluminium coating can negatively affect the detection efficiency of the scintillator.

	absolute	relative
Si PIN	273000 ± 8000	1
gas	20000 ± 4000	0.07 ± 0.02
scintillator	184000 ± 5000	0.68 ± 0.03

Table 9.2: Table of calculated absolute and relative counts of 6.4 keV photons for each detector.

The results in table 9.1 show that the scintillator detector is the best detector for 14.4 keV photons of the three detectors tested. The Si PIN detector does not excel in the detection of these energies and can be classified as the worst of the three. However, from the information provided in the S14605 data sheet [6] we conclude that the efficiency at 6.4 keV energies can be about 51 % better. This can be partially confirmed by rough estimates in the table 9.2. To measure the full peak of 6.4 keV photons with the S14605 photodiode, upgrades in the electronics have to be made to increase the SNR, mainly the preamplifier has to be optimised for the capacitance of the S14605.

Chapter 10

Mössbauer spectra measurement

The previous chapter compared the three detectors in their efficiency of detecting 14.4 keV photons. This chapter compares them in the efficiency of measuring the MS spectra. The good detection efficiency of 14.4 keV photons does not necessarily imply a good MS spectrum measurement efficiency and vice versa. Effects that do not correspond to 14.4 keV photon detection (e.g. Compton continuum) reduce the SNR of MS spectra. To determine this efficiency, a setup similar to that used for the MCA measurement is again used, with the addition of a sample with holder and transducer for Doppler energy modulation. The sample chosen for this measurement is $K_3[Fe(CN)_6]$, which is characterised by a singlet spectrum.

The whole MS setup is controlled by the Mössbauer spectrometer unit controlled by the PC software [16], both developed at DEP. The control unit drives the transducer, regulates its speed and also processes the incoming pulses from the detector. The control software also does all the data processing and acquires the MS spectrum data files that are analysed in this chapter.

The detector output is routed directly to the MS spectrometer control unit where the channel interval for the MS spectrum measurement is selected. However, the previous MCA showed that the interval of the 14.4 keV peak is different for each detector, so in order to compare the detectors in MS efficiency, the channel interval must be selected according to the location of the 14.4 keV energy peak. We selected this interval as 90% of the FWHM of the 14.4 keV energy peak with respect to the results of the MCA measurement for each detector.

The transducer is very sensitive to vibration and must therefore be placed on the anti-vibration mat together with the detector and sample holder. Before the measurement, the velocity calibration routines provided by the control software must be run on the transducer to obtain the scaling coefficient, which is then used to recalculate the velocity axis from the arbitrary units to $mm \cdot s^{-1}$.

The MS spectrum for each detector can be seen in the figures 10.1, 10.2 and 10.3. One MS spectrum was measured for 20 hours, including only the valid cycles where the velocity error did not exceed the defined limit.

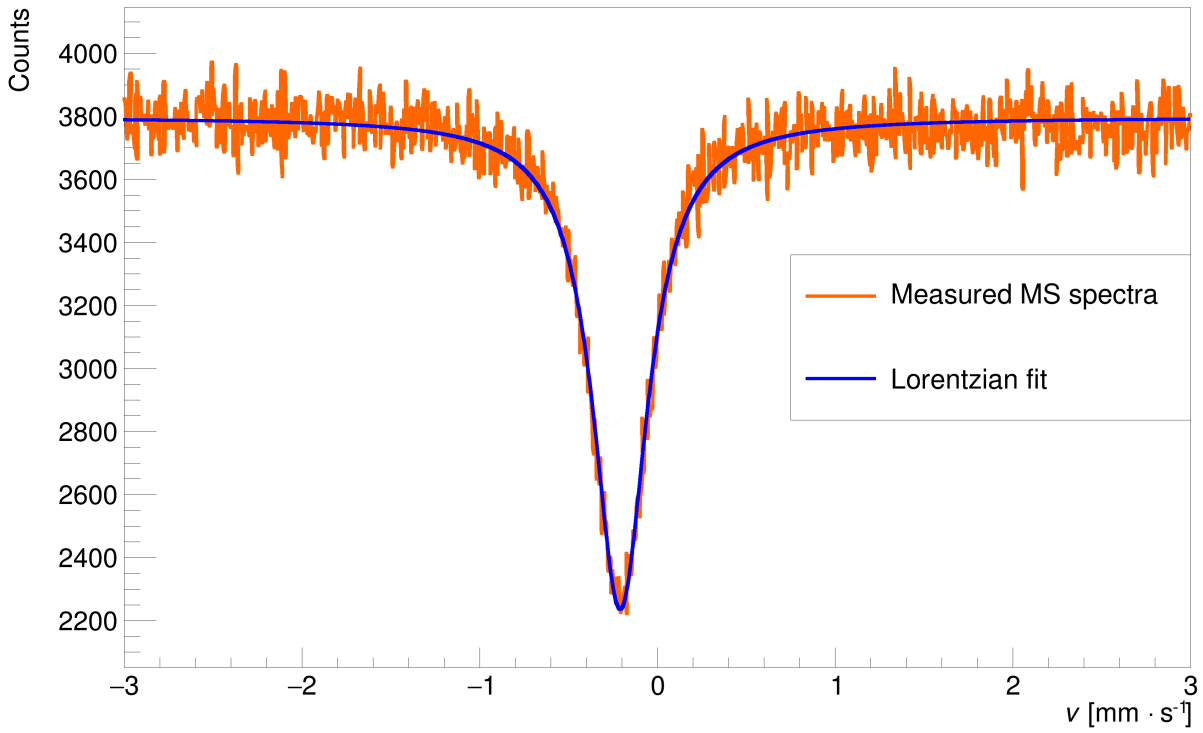

Figure 10.1: Si PIN detector $K_3[Fe(CN)_6]$ MS spectrum.

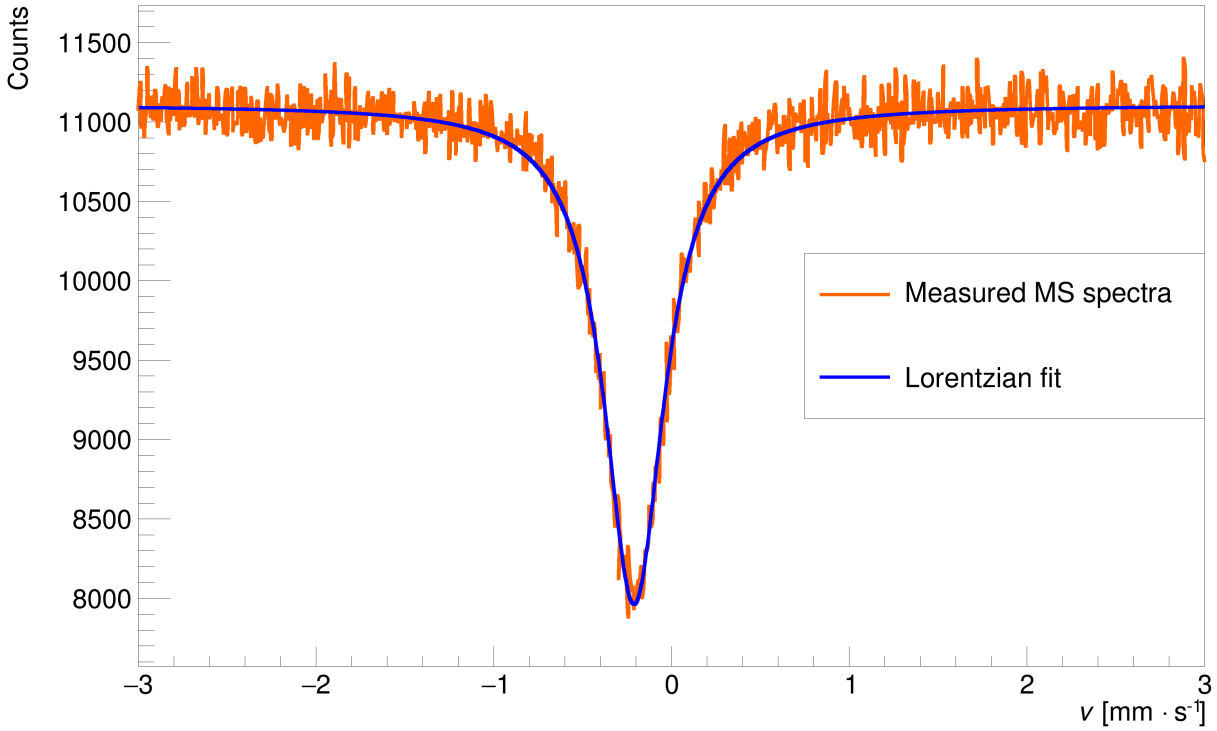

Figure 10.2: Gas detector $K_3[Fe(CN)_6]$ MS spectrum.

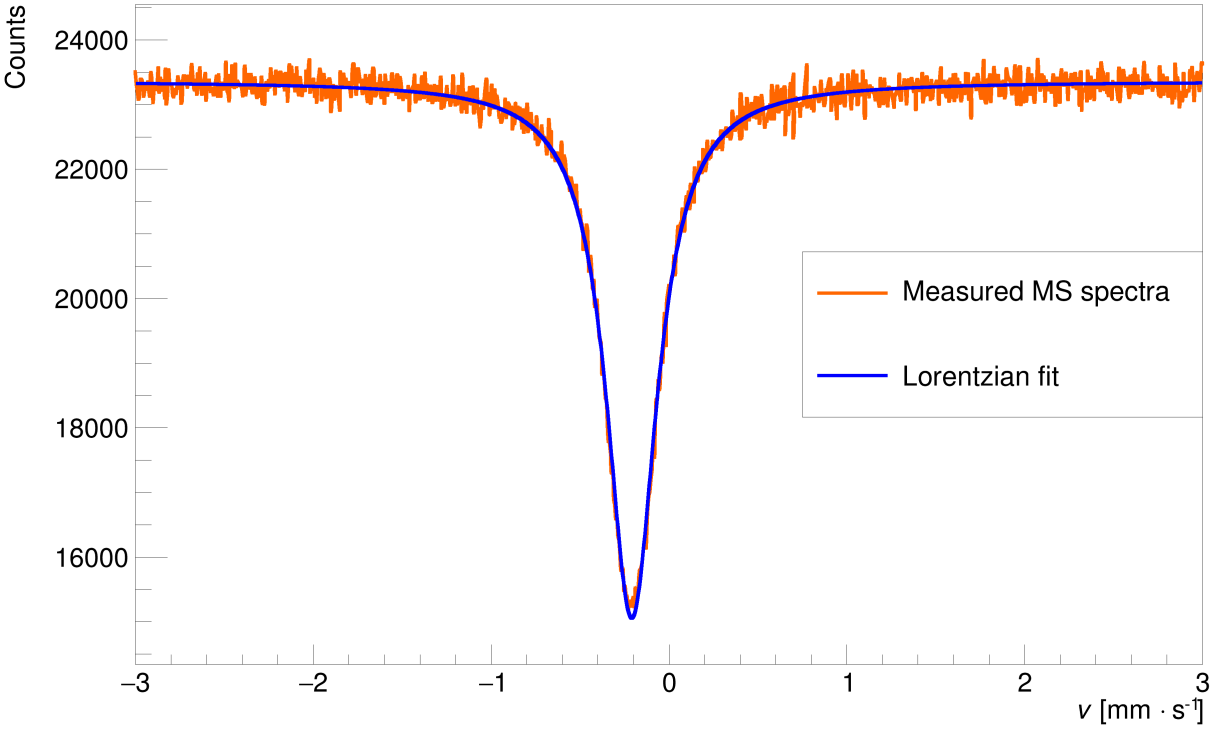

Figure 10.3: Scintillator detector $K_3[Fe(CN)_6]$ MS spectrum.

Each spectrum is fitted by the Lorentzian in the form described by the equation 4.1. However, when comparing the MS parameters between detectors, there was a problem with the different width of the line in each spectrum caused by the mechanical vibrations affecting the transducer. If the SNR_{MS} and E_{MS} (equations 4.3 and 4.4), which both depend on I_{MS}, are to be comparable between measurements, it is necessary to recalculate I_{MS} for each Lorentzian with respect to the same line width. The recalculation is based on the following consideration: The altered velocity signal may cause the variations in Γ of a singlet Lorentzian curve, but its area A (total number of counts), given by the equation 4.2, should remain unchanged by this effect. Thus, if A is conserved although Γ is changed, the new amplitudes I_{rec} corresponding to the recalculated Lorentzians with the same Γ_{ref} can be obtained by a simple relation $I_{rec} = \frac{\Gamma}{\Gamma_{ref}} I_{original}$. The reference Γ_{ref} is the lowest Γ of the spectra. The results obtained for each detector can be seen in the table 10.1.

	SNR_{MS}	E_{MS}
Si PIN	27.4 ± 0.5	0.444 ± 0.007
gas	35.7 ± 0.5	0.338 ± 0.005
scintillator	54.3 ± 0.3	0.355 ± 0.002

Table 10.1: Measured SNR_{MS} and E_{MS} for each detector.

The results show that the best SNR_{MS} is obtained with the scintillator detector, and thus the Si PIN detector is not the best candidate when it comes to acquiring MS spectra in transmission geometry. However, the highest E_{MS} is associated with the Si PIN and therefore it can be used in some applications where E_{MS} is an important parameter.

Discussion

The development of the PIN detector for transmission MS spectroscopy can be continued by using photodiodes with better detection efficiency - by using a Si photodiode with greater thickness or by using a photodiode made of another material with higher Z (e.g. Ge). To fully observe the 6.4 keV energy peak, it will be necessary to use a photodiode with lower capacitance (greater thickness also implies lower capacitance) or a preamplifier with better characteristics. This optimised preamplifier can be realised using discrete opamps. The development can also be continued by mathematical modelling of a better semiconductor detector for MS and by a theoretical simulation of its detection efficiency, using some of the well-known programs for simulating the passage of particles through matter, such as the Geant4 [31].

The semiconductor detector with a larger detection area can be made up of several PIN photodiodes. However, to reduce noise, each photodiode must have its own preamplifier and amplifier. The final aim is to build a compact Mössbauer spectrometer for backscattering geometry by combining several Si PIN photodiodes with a small transducer in one instrument.

Conclusion

The first tests of the SI PIN photodiodes were performed on a setup consisting of ORTEC modular parts. All three selected photodiodes (S14605, BPW34 and OPF430) produced spectrometric pulses and the gamma spectra of ^{57}Co were successfully measured and interpreted. Characteristic full energy peaks of ^{57}Co (14.4 keV, 122.1 keV and 136.5 keV) were observed, as well as the expected Compton continuum resulting from Compton scattering of 122.1 keV inside the detector. It was found that electromagnetic shielding plays a very important role in noise reduction. The Si PIN photodiodes attached to the charge preamplifier cannot operate properly without sufficient shielding. Cooling the photodiode also had an effect, but it was much less significant.

It was shown that even a cheap Si PIN photodiode (BPW34 and OPF430), originally designed for light detection, could be used as a detector for gamma spectroscopy. However, it has been shown that their detection efficiency is much lower than that of the S14605 photodiode, which is classified as an X-ray detector.

The analog front-end electronics, based on the Cremat preamplifier and shaper, has been successfully developed. It requires only a +15V and -15V power supply to operate. Its output can be connected directly to the MCA. The MS measurement setup using the constructed Si PIN detector was successfully assembled and the transmission MS spectra of a singlet sample were successfully measured.

Two types of measurements were performed to compare the Si PIN detector with the gas and scintillator detector - the 14.4 keV relative detection efficiency measurement and the MS measurement. The only parameter of the Si PIN detector that can be characterised as the best among the detectors tested is the effect of the measurement.

Bibliography

1. LEO, William R. *Techniques for nuclear and particle physics experiments: A how to approach*. Berlin: Springer-Verlag, 1987. ISBN 9783540572800.
2. AMPTEK. *Si-PIN vs CdTe Comparison*. Available also from: `https://www.amptek.com/internal-products/si-pin-vs-cdte-comparison`.
3. KLINGELHÖFER, G. et al. Athena MIMOS II Mössbauer spectrometer investigation. *Journal of Geophysical Research: Planets*. Vol. 108, no. E12. Available from DOI: `https://doi.org/10.1029/2003JE002138`.
4. LUTZ, Gerhad. *Semiconductor radiation detectors: Device physics*. Berlin: Springer, 2007. ISBN 9783540716785.
5. HAMAMATSU. *Si detectors for high energy particles* [online] [visited on 2023-12-26]. Available from: `https://www.hamamatsu.com/content/dam/hamamatsu-photonics/sites/documents/99_SALES_LIBRARY/ssd/high_energy_kspd9002e.pdf`.
6. HAMAMATSU. *S14605* [online] [visited on 2023-12-26]. Available from: `https://www.hamamatsu.com/content/dam/hamamatsu-photonics/sites/documents/99_SALES_LIBRARY/ssd/s14605_kpin1091e.pdf`.
7. *CERN DIY Particle Detector* [online] [visited on 2023-12-26]. Available from: `https://physicsopenlab.org/2020/06/15/cern-diy-particle-detector/`.
8. SEMICONDUCTORS, Vishay. *BPW34, BPW34S* [online] [visited on 2023-12-26]. Available from: `https://www.vishay.com/docs/81521/bpw34.pdf`.
9. RAMIREZ-JIMENEZ, F.J.; LOPEZ-CALLEJAS, R.; CERDEIRA-ALTUZARRA, A.; BENITEZ-READ, J.S.; ESTRADA-CUETO, M.; PACHECO-SOTELO, J.O. PIN diode-preamplifier set for the measurement of low-energy gamma and X-rays. *Nuclear Instruments and Methods in Physics Research Section A: Accelerators, Spectrometers, Detectors and Associated Equipment*. 2003, vol. 497, no. 2, pp. 577–583. ISSN 0168-9002. Available from DOI: `https://doi.org/10.1016/S0168-9002(02)01806-5`.
10. ELECTRONICS, TT. *OPF430* [online] [visited on 2023-12-26]. Available from: `https://cz.mouser.com/datasheet/2/414/OPF430-3241495.pdf`.
11. PROCHÁZKA, Vít. *Neobvyklá Mőssbauerova spektroskopie*. Olomouc: Palacký University Olomouc, 2014. ISBN 9788024440118.
12. BECQUEREL, Laboratoire National Henri. *Co-57*. Available also from: `http://www.lnhb.fr/nuclides/Co-57_tables.pdf`.
13. NOVÁK, Petr. *Mössbauerův spektrometr s časovým rozlišením detekce fotonů záření gama - vývoj a aplikace [online]*. 2016 [cit. 2023-11-06]. Doctoral theses, Dissertations. Palacký University Olomouc, Faculty of ScienceOlomouc.

14. NIST. *Atomic Weights and Isotopic Compositions for All Elements*. Available also from: https://physics.nist.gov/cgi-bin/Compositions/stand_alone.pl.

15. PECHOUŠEK, Jiří. *Využití techniky virtuální instrumentace při vývoji měřicích systémů pro jadernou fyziku se zaměřením na realizaci Mössbauerova spektrometru*. Brno: VUTIUM, 2014. ISBN 9788021450585.

16. STEJSKAL, Aleš. *Konstrukce duálního Mössbauerova spektrometru a adaptace pro dynamická měření [online]*. 2019 [cit. 2023-11-06]. Master's thesis. Palacký University Olomouc, Faculty of ScienceOlomouc.

17. INC, Cremat. *Advice in using Cremat CSP modules* [online] [visited on 2023-12-26]. Available from: https://www.cremat.com/applications/csp-application-notes/.

18. HAMAMATSU. *Characteristics and use of Charge amplifier*. Available also from: https://www.hamamatsu.com/content/dam/hamamatsu-photonics/sites/documents/99_SALES_LIBRARY/ssd/charge_amp_kacc9001e.pdf.

19. INC, Cremat. *CR-110-R2 charge sensitive preamplifier* [online] [visited on 2023-12-26]. Available from: https://www.cremat.com/CR-110-R2.pdf.

20. ORTEC. *Models 142A, 142B, and 142C Preamplifiers Operating and Service Manual*. Available also from: https://www.ortec-online.com/-/media/ametekortec/manuals/1/142abc-mnl.pdf.

21. ORTEC. *Introduction to Amplifiers*. Available also from: https://www.ortec-online.com/-/media/ametekortec/other/amplifier-introduction.pdf.

22. INC, Cremat. *CR-200 Gaussian shaping amplifier* [online] [visited on 2023-12-26]. Available from: https://www.cremat.com/CR-200-R2.1.pdf.

23. ORTEC. *EASY-MCA-8K EASY-MCA-2K Digital Gamma-Ray Spectrometer User's Manual*. Available also from: https://www.ortec-online.com/-/media/ametekortec/manuals/e/easy-mca-mnl.pdf.

24. MARISCOTTI, M.A. A method for automatic identification of peaks in the presence of background and its application to spectrum analysis. *Nuclear Instruments and Methods*. 1967, vol. 50, no. 2, pp. 309–320. ISSN 0029-554X. Available from DOI: https://doi.org/10.1016/0029-554X(67)90058-4.

25. ORTEC. *MAESTRO Multichannel Analyzer Emulation Software*. Available also from: https://www.ortec-online.com/products/software/maestro-mca.

26. AUTODESK. *Autodesk Eagle*. Available also from: https://www.autodesk.com/products/eagle/overview?term=1-YEAR&tab=subscription.

27. INSTRUMENTS, Texas. *Grounding in mixed-signal systems demystified, Part 1*. Available also from: https://www.ti.com/lit/an/slyt499/slyt499.pdf.

28. INSTRUMENTS, Texas. *OPA847*. Available also from: https://www.ti.com/lit/ds/symlink/opa847.pdf.

29. HAMAMATSU. *Photomultiplier tubes R6094, R6095*. Available also from: https://www.hamamatsu.com/content/dam/hamamatsu-photonics/sites/documents/99_SALES_LIBRARY/etd/R6094_R6095_TPMH1382E.pdf.

30. HAMAMATSU. *HIGH VOLTAGE POWER SUPPLY SOCKET ASSEMBLY (DP-TYPE) C9028-01*. Available also from: https://www.digchip.com/datasheets/parts/datasheet/190/C9028-01-pdf.php.

31. GEANT4. *Geant4, a toolkit for the simulation of the passage of particles through matter*. Available also from: `https://geant4.web.cern.ch/`.

List of Symbols and Abbreviations

σ	cross section
σ_{A}	cross section of single atom
F_{part}	particle flux
N_{s}	average number of particles scattered per unit time from single point target
Ω	solid angle
A	area perpendicular to the flux
N_{i}	density of interaction centres
$N_{\mathrm{sc}}(\Omega)$	average number of particles scattered per unit time multiple interaction centres
N_{tot}	average number of particles scattered per unit time multiple interaction centres integrated over entire solid angle
δx	material thickness
Z	atomic number
I_{T}	transmitted radiation intensity
I_0	incident radiation intensity
μ	total absorption coefficient
N_{d}	atomic density
N_{a}	Avogadro number
ρ	material density
A_{w}	molecular weight
f	photon frequency
h	Planck's constant
$\hbar$	reduced Planck's constant
E_{e}	kinetic energy of free electron
E_{b}	binding energy of electron
E_2	scattered photon energy
E_1	initial photon energy
m_{e}	electron mass
M	heavy charged particle mass
c	speed of light in vacuum
$\frac{dE}{dx}$	stopping power
θ	scattering angle
φ	maximum scattering angle
E_{c}	energy of electron inside crystal
$E_{\mathrm{c}}(\boldsymbol{k})$	energy dispersion relation
$\boldsymbol{k}$	wave vector
E_{g}	energy gap
E_{T}	thermal energy
E_{s}	electrostatic energy
E_{photon}	photon energy

E_{F}	Fermi level energy
k	Boltzmann constant
ϕ	electrostatic potential
T	thermodynamic temperature
t	temperature (Celsius scale)
ω_{photon}	photon angular frequency
E_{gamma}	incident gamma photon energy
ϵ	average energy for electron-hole pair generation
n	number of generated electron-hole pairs
E	energy of incoming particle
F	Fano factor
U_{R}	reverse voltage
E_0	base energy level of nucleus
E_{M}	pertubed energy level of nucleus
Q_{n}	quadrupole momentum of nucleus
m	nuclear magnetic number
I_{n}	spin of nucleus
E_{Q}	energy variation with respect to magnetic quantum number
γ	gyromagnetic ratio
δ	isomer shift
μ_{m}	magnetic momentum of nucleus
L_{v}	Lorentzian in MS spectrum
v	relative velocity of radiation source and MS sample
v_0	resonant velocity
A	area under Lorentzian
Γ	FWHM of Lorentzian
I_{MS}	amplitude of Lorentzian
B	MS background level
E_{MS}	MS effect of measurement
$\mathrm{SNR}_{\mathrm{MS}}$	MS signal to noise ratio
Q	charge
U	voltage
I	current
I_{G}	FET gate current
I_{D}	dark current
C_{f}	feedback capacitance
R_{f}	feedback resistance
G	gain
en_1	thermal noise of the first stage FET
en_2	thermal noise caused by feedback resistance
in	shot noise
$noise$	total noise
ω	signal angular frequency
j	complex unit
g_{m}	FET transconductance
τ	decay constant
U_{A}	pulse amplitude
C_{in}	input capacitance
C_{j}	detector capacitance

C_s	amplifier input capacitance
d	collimator diameter
I_rec	recalculated amplitude of Lorentzian
I_original	original amplitude of Lorentzian
Γ_ref	original FWHM of Lorentzian
$\mathrm{FWHM}_\mathrm{CR\text{-}100}$	FWHM limit given by CR-110
$\mathrm{FWHM}_{14.4}$	FWHM of the 14.4 keV peak
$\mathrm{FWHM}_\mathrm{Fano}$	FWHM given by fano noise

PCB	printed circuit board
SNR	signal to noise ratio
PMT	photomultiplier tube
DEP	Department of Experimental Physics
MCA	multichannel analyser
APD	avalanche photodiode
CCD	charge-coupled device
CMOS	complementary metal–oxide–semiconductor
FWHM	full width at half maximum
GND	ground
YAP(Ce)	yttrium aluminium perovskite dopped by cerium
MS	Mössbauer spectroscopy
MPC	model predictive control
PID	proportional–integral–derivative

Appendix

Schematic and layout of the integrated amplifier

Full EAGLE schematic and layout are in the folder IntegratedAmplifier.

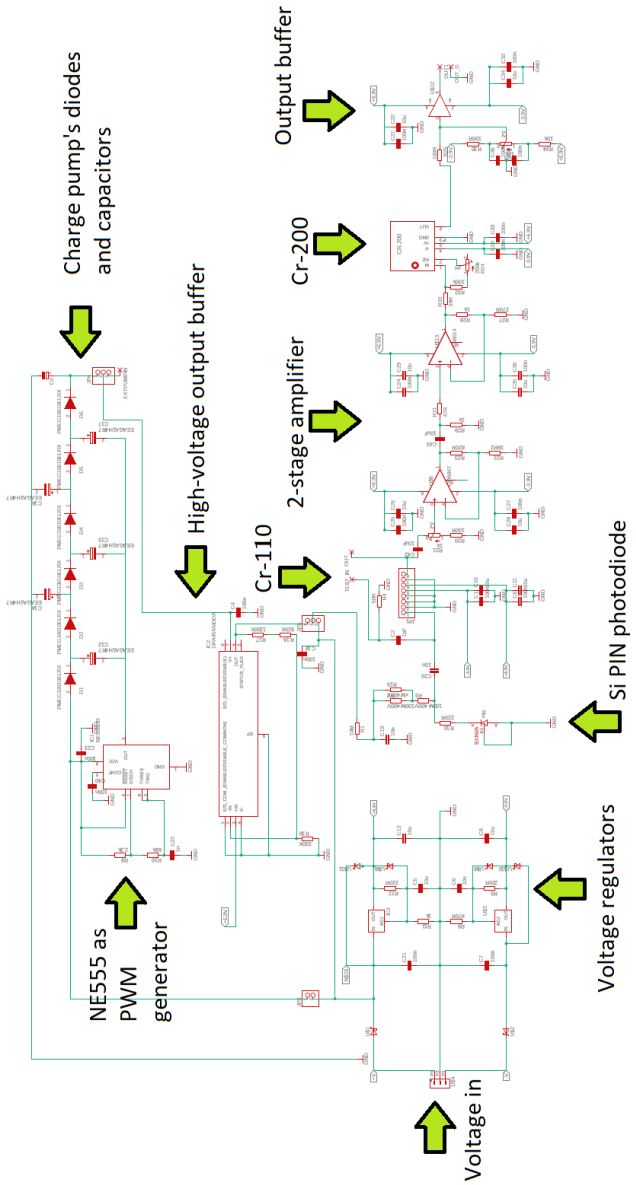

Schematic of integrated amplifier.

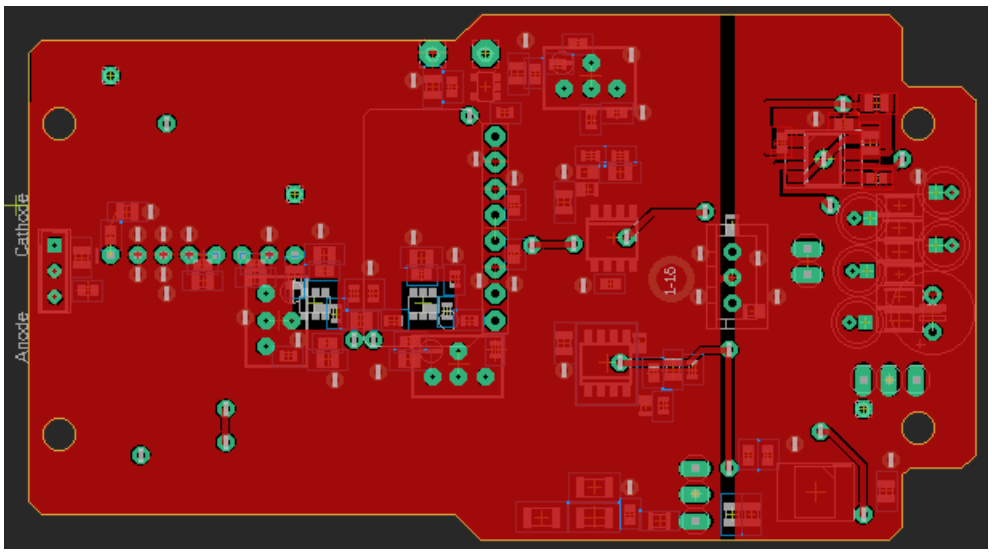

Layout of integrated amplifier, top side layer.

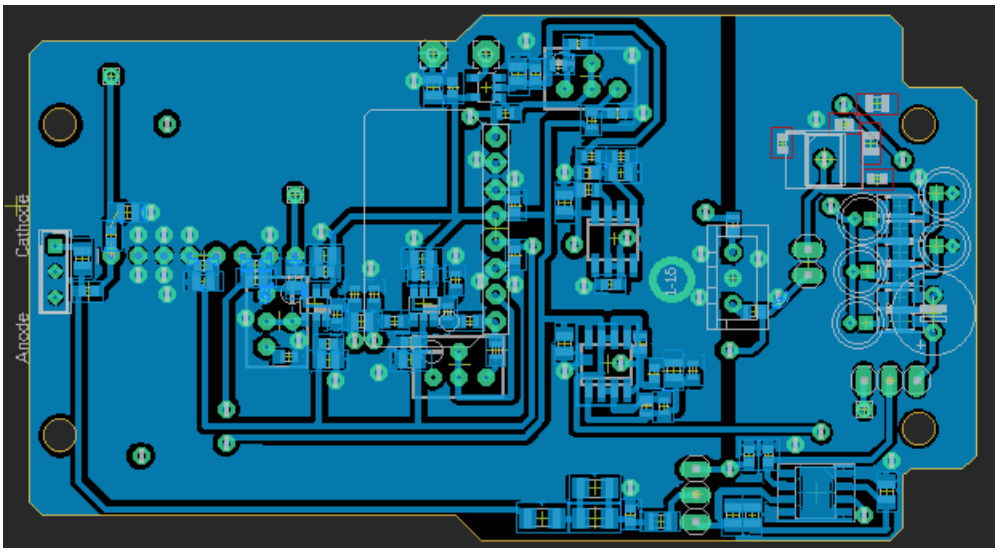

Layout of integrated amplifier, bottom side layer.

Peak searching program

File SpectreAnalyzer.cpp: C++ program for automatic searching of peaks in spectrum.